Cobalt-Hexamine (HMT) Metal-Organic Framework-derived Bifunctional Electrocatalyst for Oxygen Reduction and Evolution Reactions

by

Yue Niu

A thesis

presented to the University of Waterloo

in fulfillment of the

thesis requirement for the degree of

Master of Applied Science

in

Chemical Engineering

Waterloo, Ontario, Canada, 2019

Author's Declaration

I hereby declare that I am the sole author of this thesis. This is a true copy of the thesis, including any required final revisions, as accepted by my examiners.

I understand that my thesis may be made electronically available to the public.

Abstract

With the high requirement of increasing people's living standards and building a more sustainable society, electrochemical energy storage devices with large energy density, high power density, and long term durability are greatly needed to mitigate the consumption of fossil fuels. Among all those well-known energy storage systems, zinc-air batteries are one of the most appealing candidates due to sufficient and inexpensive resources applied, promising energy density, as well as the high reduction potential of zinc. However, Zn-air batteries always suffer from relatively high overpotential, which is predominantly originated from the sluggish kinetics of oxygen electrocatalytic reactions. Enormous efforts have been devoted to the development of active bifunctional electrocatalysts for oxygen reduction reaction (ORR) and oxygen evolution reaction (OER).

Although noble-metal catalysts, such as platinum, iridium, and their alloys have been proved to own outstanding electrochemical performances for oxygen electrocatalysis, their insufficient catalytic bifunctionality, rarity and high cost hinder the commercial utilization. As a result, the design and synthesis of cost-effective, robust and highly stable bifunctional electrocatalysts to replace noble metal catalysts for zinc-air batteries are greatly desirable to realize the commercialization of Zn-air batteries. In recent years, the metal-organic frameworks (MOFs) are burgeoning as attractive precursors for the fabrication of transition-metal-based bifunctional oxygen electrocatalysts with controllable nanostructures due to the structural and compositional advantages of the MOF.

Herein, a layered Co-hexamine coordination framework is prepared and used as an efficient precursor to synthesize high-performance ORR/OER bifunctional electrocatalyst featured with cobalt oxide and cobalt phosphide heterostructured structure (denoted as CoO/Co_xP). This design not only generates a high surface area to expose more active sites but also guarantees the excellent bifunctionality by integrating the cobalt phosphide and cobalt oxide, which are specifically active to OER and ORR, respectively. Moreover, the synergistic effects of these nanoparticles, as well as the superior structural features, can further boost the catalytic activities. As a result, CoO/Co_xP outperforms the state-of-art non-noble metal catalysts and the noble metal benchmark with a half-wave potential of 0.86 V for ORR and a low potential of 1.60 V to generate a current density of 10 mA cm^{-2} for OER. The promising bifunctional catalytic activity thus makes it highly promising to be implemented in rechargeable Zinc-air battery.

Acknowledgements

The work reported herein was financially supported by the University of Waterloo.

The author would like to thank Dr. Zhongwei Chen and Dr. Aiping Yu for their meticulous guidance and helpful support on my Master's study. A special thanks to Dr. Meiling Xiao for working closely with me and providing me with valuable advice and assistance.

I would also like to thank my family for their consistent love and support for me.

Many thanks to the author's colleagues including Dr. Zhengyu Bai, Dezhang Ren, Fei Lu, Jianbing Zhu, Rui Lin Liang, Ruidi Liu, Wenwen Liu, Wenyao Zhang, Ruohan Jiang, Ting Huang, Xiaoyuan Dou, Yanfei Zhu, Yatian Zhang, Zhaoqiang Li, Zhen Zhang, Ya-Ping Deng, Abel Sy, Gaopeng Jiang , Gaoran Li, Guihua Liu, Guobin Wen, Dan Luo, Hao Liu, Haozhen Dou, Jiahua Ou, Jile Fu, Jing Zhang, Jun Geun Um, Kaliyappan Karthikeyan, Kiyoumars, Lei Zhao, Mahboubehsadat Mousavi, Maiwen Zhang, Mohd Altamash Jauhar, Moon Park, Pan Xu, Qian Li, Qing Chen, Ricky Tjandra, Saeed Habibpour, Sahar Hemmati, Sepehr Khazraei, Stephen, Storm William Gourley, Tyler Or, Xiaogang Fu, Yalin Wu, Yan Liu, Yi Jiang, Yi Pei, Yining Zhang, Youlin Liu, Yun Zheng, Zachary Paul Cano, and many other colleagues for their kind help.

Moreover, I would like to acknowledge support from my reviewers, including Professor Zhongwei Chen, Professor Eric Croiset, Professor Jeff Gostick.

Table of Contents

List of Figures

List of Tables

List of Abbreviations

ZIF	**Zeolitic imidazolate framework**
MOFs	**Metal-organic framework**
TEM	**Transmission electron microscopy**
HRTEM	**High-resolution transmission electron microscopy**
SEM	**Scanning electron microscopy**
XRD	**X-ray diffraction**
XPS	**X-ray photoelectron microscopy**
LSV	**Linear sweep voltammetry**
CA	**Chronoamperometric**
ORR	**Oxygen reduction reaction**
OER	**Oxygen evolution reaction**
SHE	**Standard hydrogen electrode**
RHE	**Reversible hydrogen electrode**
SCE	**Saturated calomel electrode**
RDE	**Rotating disk electrode**
K-L	**Koutecky-Levich**
BV	**Bulter-Volmer**
$\mathbf{E_{onset}}$	**Onset potential**
$\mathbf{E_{j=10}}$	**Potential at 10 mA cm^{-2}**

$E_{1/2}$	**Half-wave potential**
TM-N-C	**Transition metal-nitrogen carbon**
EELS	**Energy-loss spectrum of electron-energy-loss spectroscopy**
SAED	**Selected area electron diffraction**

1. Introduction

Over the past decades, the continuous consumption of energy, the environmental pollution as well as the exhaustion of fossil fuels prompts the development of alternative energy storage and conversion systems such as Li-ion batteries, fuel cells, metal-air batteries, etc[1, 2]. Since the electrochemical batteries have been successfully applied in portable devices in the 1990s, the fast development of smart devices and electric vehicles technologies pave the way to invent more powerful, stable, and efficient energy storage systems[3]. Among various kinds of batteries, the rechargeable metal-air battery is one of the most satisfactory choices for its high energy density, low cost and the plentiful fuel, air.[4, 5]. Because the cathode of a metal-air battery is air without a solid electrochemical active material loaded on the electrode, the metal anode is the key factor to determine the capacity of the metal-air battery. Among various options of metals with the potential of serving as the metal anode, Li and Zn have attracted most of the interests of researches[5]. Unfortunately, Li-O_2 battery requires an inert atmosphere to prevent the highly reactive Li metal anode from reacting with the moisture in the air during the process of fabrication and operation

Moreover, the organic electrolytes of most Li-air battery systems are expensive and flammable[6]. By contrast, zinc with the advantages of having decent energy density (1218 Wh kg^{-1}), abundant and non-precious zinc metals could be a more suitable metal anode[7]. Moreover, Zn-air batteries possess other positive properties such as using more economical and eco-friendly aqueous electrolytes, having suitable working voltage (~1.66 V), intrinsic safety, etc[8].

Even though the reactions between metals and oxygen are spontaneous, the sluggish kinetics of the oxygen reactions at the cathode usually cause large overpotential during charging and discharging process which retards the commercialization of Zin-air batteries. To overcome the kinetic issue, catalysts are necessitated to accelerate oxygen electrocatalysis. Noble metals like Ir, Ru, Pt, and their composites are commonly recognized as the efficient catalysts due to their outstanding catalytic performance[9]. However, the high cost and limited reserves of noble metals restricted their widespread application. Motivated by this challenge, substantial researches have been done to exploit inexpensive alternatives such as transition metal oxide catalysts[10-12], transition metal phosphide catalysts[13-15], perovskite catalysts[16], layered metal hydroxide catalysts[17], etc.

Metal-organic frameworks (MOFs) are a class of crystalline compounds consisting of metal ions coordinated to organic ligands to form one-, two-, or three- dimensional materials with well-defined morphologies, large specific surface area, and well-dispersed metal nanoparticles. The unique compositional and morphological features enable MOF and MOF-derived materials to be utilized as functional materials for energy conversions based on ORR, OER, HER electrocatalysis, etc[18-20]. In recent years, emerging works have proved that the advantages of intrinsically good reactivity, optimized electronic conductivity, and boosted ionic and gas diffusion of MOF-derived catalysts help to improve the bifunctionality of the electrocatalysts[21, 22].

In this work, Cobalt(II) nitrate hexahydrate serves as the source of metal ions, while hexamine acts as an organic ligand, and the derived Co-hexamine coordination framework is then utilized as an efficient two-dimensional precursor. A following low-temperature phosphorization method was carried out to synthesize CoO/Co_xP heterostructured nanoparticles. This design combines the

advantages of cobalt phosphide and CoO, which possess excellent OER and ORR activity, respectively. Besides, the synergistic effects of these nanoparticles, as well as the superior structural features, promote the catalytic activities. Detailed results and analysis will be presented in the results and discussion section.

1.1. Thesis Organization

Section 2 will describe the fundamental knowledge of oxygen reduction reaction, oxygen evolution reaction. Besides, MOF and MOF-derived bifunctional electrocatalysts will be demonstrated by order of classification, following with a short literature review.

Section 3 will include all of the characterization techniques applied to obtain the results. The characterization methods consist of physical characterization techniques, such as TEM, SEM, XRD, and XPS, as well as electrochemical characterization techniques, for example, LSV.

Section 4 describes the motivation of designing the Co-HMT-derived CoO/Co_xP heterostructure catalyst and the experimental methods. And then Section 5 provides the results and corresponding discussion. As the last part of the thesis, Section 6 presents the conclusion of the project and posts future works.

2. Background

2.1. Oxygen Reduction Reaction

2.1.1. Mechanism of ORR

Oxygen reduction reaction has been extensively investigated over the last century for it plays an important role in energy conversion, particularly in the field of metal-air batteries and fuel cells. In general, the ORR in the cathode of zinc-air battery proceeds through the following steps:

(1) O_2 diffuses and adsorbs on the surface of catalyst;

(2) Electrons transfer from anode to the cathode and O_2 is reduced at the catalyst/oxygen interface;

(3) The reduction product desorbs from catalyst surface and then transfers to the zinc anode via the electrolyte

Regarding the exact mechanism of the oxygen reduction reaction, oxygen reduction in aqueous solution mainly follows two different pathways: either a direct 4-electron reduction pathway from oxygen to water or an indirect 2-electron reduction pathway from oxygen to peroxide. For the indirect pathway, the unfavorable intermediate product of corrosive peroxide may cause low electrochemical energy efficiency and instability[23-25]. The other direct 4-electron pathway is considered to be the most desirable way. The competition of these two pathways is highly associated with the selectivity of the catalyst[26]. And from the zinc-air battery point of view, ORR catalysts with high 4-electron pathway selectivity are critical for batteries achieving high

working efficiency and energy density[27].

The thermodynamic potential values of ORR is various at different pH values. Thus, the reaction can be presented in different forms relying on the medium at which the reaction takes place. At the alkaline electrolyte, two different pathways can be written as follows (all of the potentials are versus SHE):

$$O_2(g) + 2H_2O(aq) + 4e^- \rightarrow 4OH^-(l) \qquad E^0 = +0.401\ V \qquad (1)$$

$$O_2(g) + H_2O(aq) + 2e^- \rightarrow HO_2{}^-(l) + OH^- \qquad E^0 = -0.076\ V \qquad (2)$$

At the acidic medium, oxygen reactions are represented as the equation (3) and equation (4):

$$O_2(g) + 4H^+(aq) + 4e^- \rightarrow 2H_2O(l) \qquad E^0 = +1.229\ V \qquad (3)$$

$$O_2(g) + 2H^+(aq) + 2e^- \rightarrow H_2O_2(l) \qquad E^0 = +0.670\ V \qquad (4)$$

For peroxides produced in 2-electron transfer pathway, they are unstable and can be further reduced in the acidic solution (equation (5)), and in the alkaline electrolyte (equation (6)):

$$H_2O_2(aq) + 2H^+(aq) + 2e^- \rightarrow 2H_2O(l) \qquad E^0 = +1.770\ V \qquad (5)$$

$$H_2O(l) + HO_2{}^-(aq) + 2e^- \rightarrow 3OH^-(aq) \qquad E^0 = +0.870\ V \qquad (6)$$

Because catalyzed ORR is a multi-step reaction, investigating the rate-determining step is more meaningful than the overall reaction rate. In general, one typical mechanism for the oxygen reduction reaction occurs in the alkaline electrolyte has been presented for metal-based electrocatalysts, which involves the formation of several intermediates including O_2*, HOO*, O*, and HO* (* represents a single surface active site):

$$* + O_2 \rightarrow O_2 * \qquad (7)$$

$$O_2 * + H_2O + e^- \rightarrow HOO * + OH^- \qquad (8)$$

$$HOO* + e^- \rightarrow O* + OH^- \quad (9)$$

$$O* + H_2O + e^- \rightarrow HO* + OH^- \quad (10)$$

$$HO* + e^- \rightarrow OH^- \quad (11)$$

The generation of those oxygenated adsorbates plays a vital role in determining the catalytic performance. A French chemist Paul Sabatier presented a qualitative concept in electrocatalysts named Sabatier principle. As described in principle, a promising catalytic activity requires neither too strong nor too weak interactions between the catalysts and the substrates[28]. Extremely strong interactions result in the low substrate, intermediates, or products dissociation rates. Thus, further reactions will not be available on the catalytic surface. On the other hand, too weak interactions hinder the formation of chemical bonds between the catalyst and substrate, hence no reaction will happen. Therefore, obtaining the energy barriers of different elementary reaction steps mentioned above is important for identifying the rate-determining step of the overall ORR. However, it's unpractical to get the energy barriers by the experimental method, and researchers usually accomplish them via computational methods, for example, the density functional theory[29, 30].

Specifically, the oxygen reaction electron-transfer number is calculated by the Koutecky-Levich (K-L) equation, which is described as equation (26) and equation (27) in the experimental section. The K-L equation expresses the relationships between the measured electric current density form an electrochemical reaction and the kinetic activity as well as the mass transport of reactants. Since the loading on the electrode is low enough, the actual reactive surface area can be approximately equal to the area of the electrode. Thus, the equation includes the terms of measured current, the kinetic current, and the mass transport current. Among them, the kinetic current can

be modeled by BV equation, while the mass transfers current relies on the electrochemical setup and amount of stirring. Generally, the data is collected by measuring the current at different rotation speeds. As shown in Figure 1, the inverse measured current is plotted versus the inverse square root of rotation speeds. The slope represents the inverse Levich constant, and then the electron-transfer numbers can be obtained by extrapolating the equation (27).

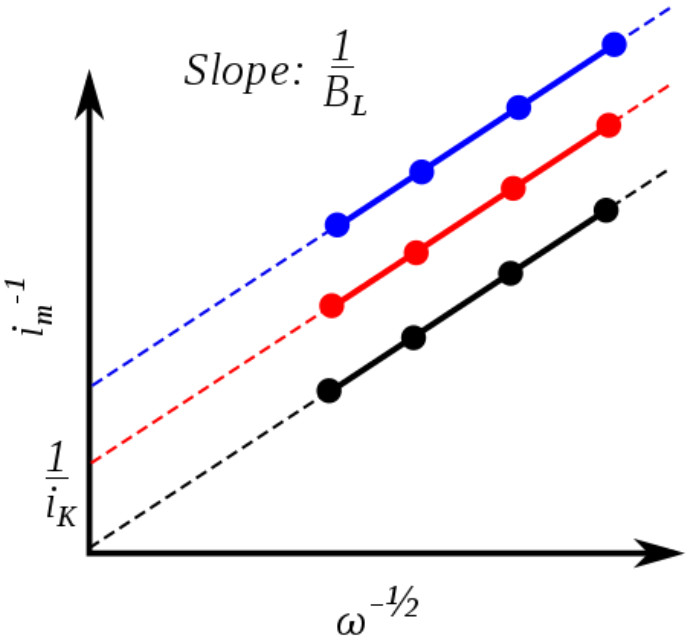

Figure 1: Koutecky-Levich plots

2.1.2. Kinetics of ORR

It's desirable for the ORR to take place at a potential close to the thermodynamic potential. To get close to the thermodynamic potentials, the charge transfer kinetics for oxygen reduction reaction must be as quick as possible. In electrochemistry, the over-potential usually used to

describe the kinetics of reactions. Overpotential stands for the potential difference between a thermodynamically determined reduction potential of a half-reaction and the potential where the redox event is experimentally obtained[31]. For ORR, the onset potential is a very important index used to define the over-potential of redox reaction occurring on the surface of the electrodes modified by catalysts, the equation shows as follows:

$$\eta = E_{onset} - E_{eq} \tag{12}$$

in which E_{onset} represents the potential at which the ORR current starts to rise and E_{eq} is the equilibrium potential. The difference η is called over-potential or polarization. There are three distinct types of over-potential (polarization) as shown in equation (13):

$$\eta = \eta_{act} + \eta_{conc} + iR \tag{13}$$

in which:

η_{act} is the activation over-potential (polarization), which is the potential difference describing the electron transfer kinetics of an electrochemical reaction, so it can also be called "electron transfer potential".

η_{conc} is the concentration over-potential (polarization). This potential difference is induced by the concentration differences of charge-carriers between solution and the electrode surface. η_{conc} describes the mass transfer limitations related to the electrochemical process.

iR is the resistance over-potential. This function includes aspects of surface polarization capacitance, electrolyte diffusion, as well as some other counter electromotive forces.

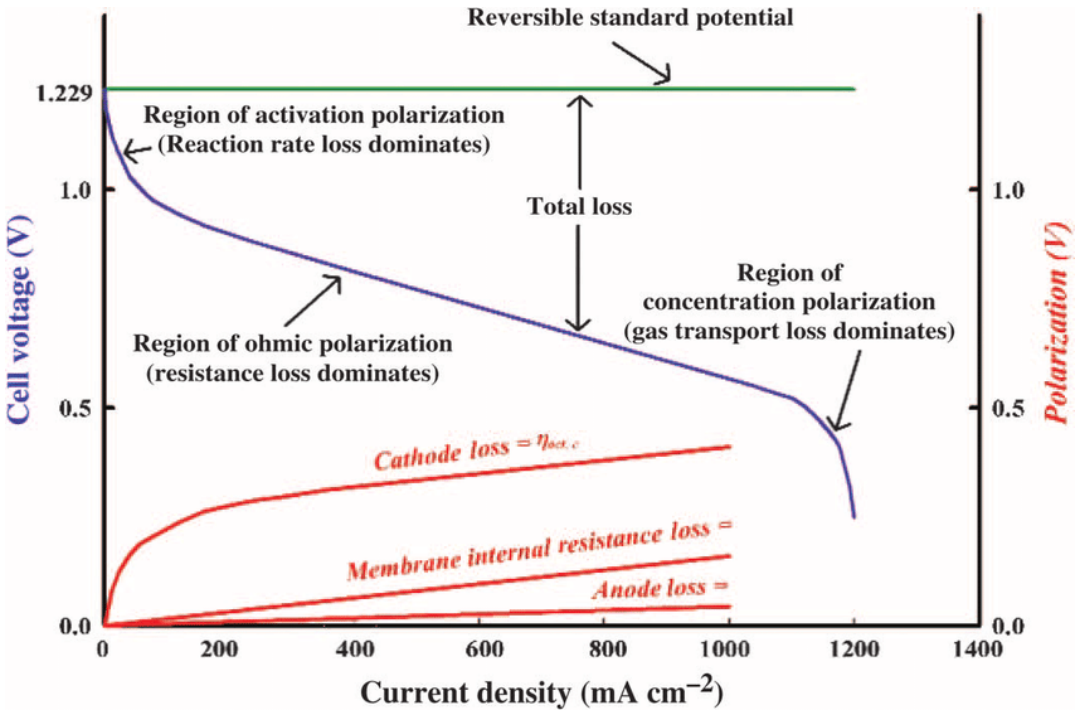

Figure 2: Diagram shows the polarization curve of PEMFC[32]

As shown in Figure 2, η_{act} is present and most dominant at small polarization current density. As for the η_{conc}, it's always predominant at large polarization current density, in this region, the reaction rate relies on the ability of charge-carriers to diffuse to the electrode surface.

The Butler-Volmer (BV) equation (equation (14)) describes the relationship of the over-potential and the net current at equilibrium, which is one of the most fundamental relationships in electrochemistry.

$$j = j_0 \left\{ exp\left(\alpha \frac{nF}{RT}\eta\right) - exp\left(-[1-\alpha]\frac{nF}{RT}\eta\right)\right\} \quad (14)$$

where j stands for the ORR current density, j_0 is the exchange current density as the current density in both the cathodic and anodic directions at the equilibrium potential, n is the electro-transfer number during the reaction process, α is the transfer coefficient, η is the over-potential mentioned above, F is the Faraday constant, R is gas constant, T is the Kelvin temperature.

The two terms of BV equation reflect the low over-potential (η_{conc}) region and the high over-potential (η_{act}) region, respectively. What's more, because of the irreversibility nature of oxygen reactions, the generated reaction currents at higher over-potentials are more appropriately be presented as:

$$j_a = j_0 exp\left(\alpha \frac{nF}{RT}\eta\right) \tag{15}$$

$$j_c = -j_0 exp\left(-\alpha \frac{nF}{RT}\eta\right) \tag{16}$$

in which the subscripts "a" and "c" stand for anodic and cathodic, respectively.

And then the BV equation can simplify to the Tafel equation which is specifically the semilogarithmic form of equation (15) and (16), as shown in equation (17):

$$\eta = \frac{RT}{\alpha F} lnj_0 - \frac{RT}{\alpha F} lnj = a - blnj \tag{17}$$

where:

a and b are Tafel constants (for a given reaction and temperature), the values of these constants usually depend on the properties of the material, the condition of the electrode surface, the electrolyte components, temperature, and so on. Tafel equation plays an important role in the determination of the kinetics of the electron-transfer process. A plot of over-potential versus lnj known as the Tafel plot, thus, the constant b is also called Tafel slope. The value of Tafel slope is reaction mechanism indicator, which can directly provide the information to judge the catalytic activity. Usually, the smaller the value of the Tafel slope, the better the oxygen reaction activities. On the other hand, with higher Tafel slope, the over-potential increases faster with current density.

2.1.3. Other Important Concepts of ORR

Figure 3. demonstrates a typical ORR polarization curve, from which several ORR kinetics performance indicators are indicated.

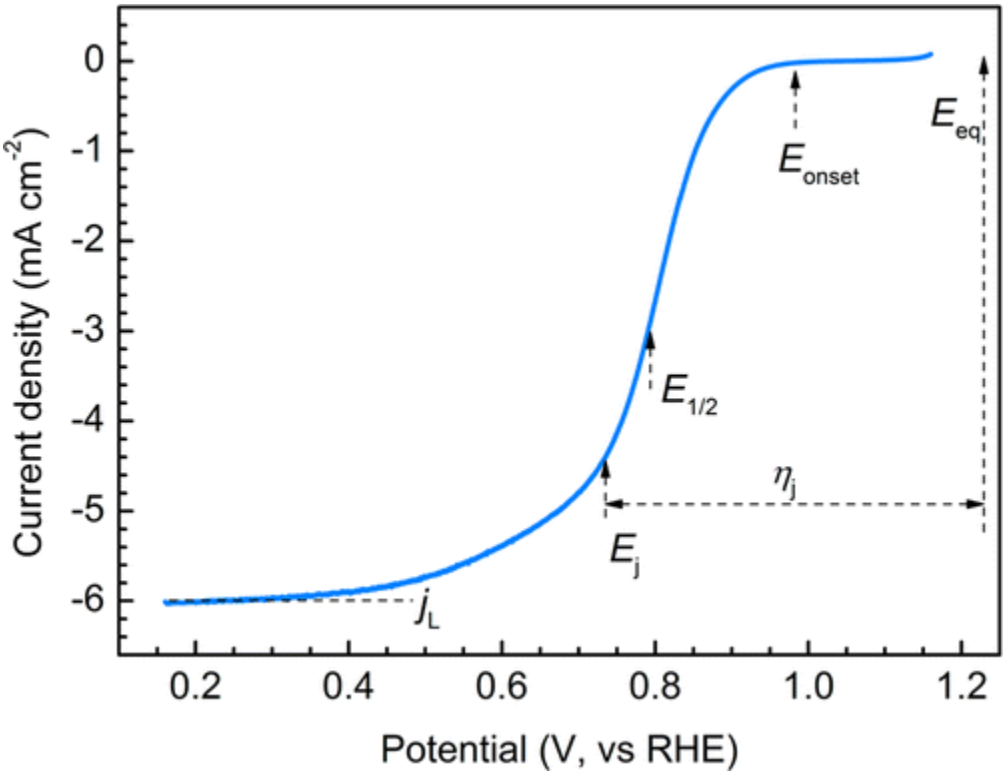

Figure 3: Typical ORR polarization curve of Pt/C catalyst from RDE system[33]

j_L is the diffusion-limiting current density, it occurs at the concentration polarization region. Under j_L, the reactant concentration on the electrode surface close to zero, which means the oxygen reaches the fastest diffusion rate. According to equation (20), for a certain electrode reaction (electron-transfer number as a constant), the diffusion-limiting current density is only determined by the rotation speed. As a result, for different materials, the oxygen reductions take place via different pathways which will reflect on the electron-transfer numbers, resulting in

different diffusion-limiting current densities. In conclusion, j_L is the intrinsic property of certain catalyst material. Usually, the higher j_L observed, the higher the current flow through the unit area, the faster the reaction dynamics.

The onset potential (E_{onset}) is usually defined as the potential at the current density of 0.1 mA cm^{-1}, while the half-wave potential ($E_{1/2}$) is the potential at the half diffusion-limiting current density. Both of these potentials are intrinsically the same, which are applied to measure the over-potential of the reaction. However, the onset potential describes more about the thermodynamics of the reactions, while the half-wave potential reflects comprehensive activities of the electrocatalysts from the thermodynamic and kinetic aspects.

2.2. Oxygen Evolution Reaction

The evolution of oxygen in the alkaline electrolyte is a relatively ambiguous process, and thus, the reaction pathways differ according to the catalysts and active sites[34]. Generally accepted OER reaction mechanisms comprise the reverse process of ORR via four consecutive protons and electron transfer steps[35]. The mechanisms equations are presented below:

$$* + OH^- \rightarrow OH* + e^- \quad (18)$$

$$HO* + OH^- \rightarrow O* + H_2O + e^- \quad (19)$$

$$O* + OH^- \rightarrow HOO* + e^- \quad (20)$$

$$HOO* + OH^- \rightarrow O_2* + H_2O + e^- \quad (21)$$

$$O_2* \rightarrow * + O_2 \quad (22)$$

For the oxygen reduction reaction, it occurs at the three-phase interface of catalyst-oxygen-electrolyte. As for the oxygen evolution reaction, the mechanism mainly revels at a two-phase reaction zone (oxide surfaces and oxidized metal surfaces). The reaction kinetics of OER is similar to the ORR, which is greatly controlled by the binding energy of adsorbing oxygen species on the reactive sites. Understanding the relations of the oxygen evolution reaction activities and the difference of binding strengths between oxygen intermediates of various classes of catalyst materials through theoretical calculation can help to develop active electrocatalysts for OER[36].

The sluggish four-electron transfer process of OER and the difficult oxygen-oxygen double bond formation are the main bottlenecks of improving OER efficiency, which requires active electrocatalysts. The state-of-the-art oxygen evolution catalyst are noble-metal-based catalysts, such as Ir, Ru, IrO_2, and RuO_2, but are fairly expensive. It's highly impressive to replace these high-cost noble metal catalysts by a class of catalyst materials consisting of transition-metal oxides and phosphides[37]. For these materials, surface metal cations usually serve as the OER active sites, which can combine with those oxygen species during the OER to form stable intermediates. These intermediates on the metal surfaces generate the activation barriers, which influence the rate-determining step and then the OER rates.

Analogous to the ORR, the OER performances are judged by the overpotential and Tafel slope. The potential at a current density of 10mA cm^{-2} is the criterion to evaluate the thermodynamic performances of different OER catalysts, thus, the overpotential of oxygen evolution reaction is the difference between this criterion potential and standard hydrogen potential. On the other hand, as reported in the ORR section, the value of the Tafel slope is the reaction mechanism indicator,

which can directly provide the information to judge the OER catalytic activity. Similarly, the smaller Tafel slope indicates better catalytic kinetics.

2.3. MOF-Derived Bifunctional ORR&OER Catalysts

Most of the MOF-derived oxygen electrocatalysts are carbon-based catalysts with satisfying electronic conductivity and structural porosity. The advantages and shortcomings of three main types of MOF-derived materials and their design methodologies are demonstrated in Figure 4[2].

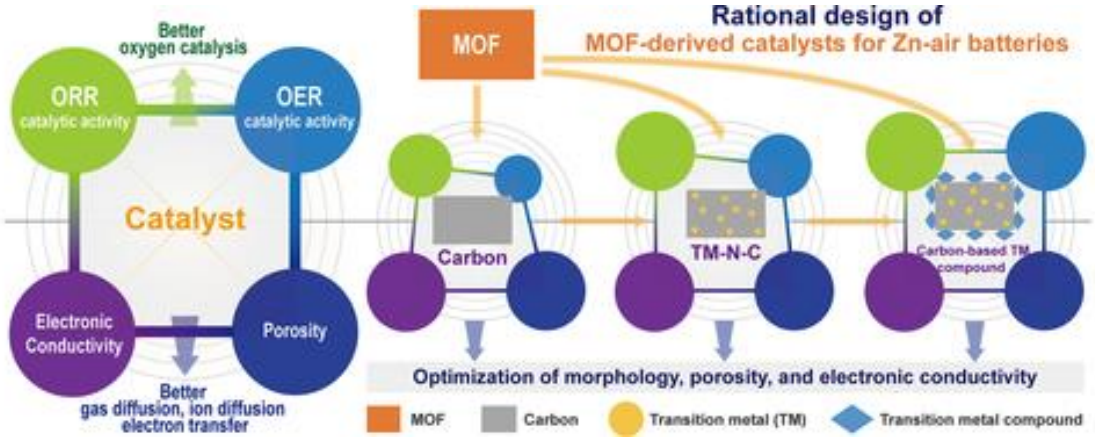

Figure 4: Illustration of the benefits and drawbacks of MOF-derived oxygen catalysts and the developing strategies[2]

As we can see from the image, carbon-based MOF-derived catalyst usually have promising electronic conductivity and high porosity. Specifically, Metal-free carbon catalysts are lacking ORR and OER activities. As for the transition metal-nitrogen-carbon catalysts, they always demonstrate satisfactory ORR catalytic activity while poor OER activity. The carbon-based transition metal compound catalysts outperform these three types of catalysts by their promising

bifunctionality. In the next part of this section, literature reviews will be presented.

2.3.1. Transition Metal-Nitrogen-Carbon Composites

This type of catalyst consists of transition metal-nitrogen-carbon materials, transition metal alloys, and even single transition metal atom catalysts. In 2016, Xia's group reported a method to convert Co-ZIF-67 into a high graphitized degree hollow framework consisting of cobalt particles decorated N-doped CNT frameworks[38]. A void-abundant and N-doped CNTs frameworks shell is synthesized by the calcination of the ZIF precursor. The as-prepared catalyst exhibited lower ORR overpotential than commercial Pt/C catalyst. This work paved the way of designing various MOF-derived transition metal-nitrogen-carbon composites bifunctional electrocatalysts.

Among all the TM-N-C mono-functional catalyst materials, Co-N-C materials are well investigated for bot oxygen reduction reaction and oxygen evolution reaction applied for either primary or rechargeable zinc-air batteries. Co-N-C electrocatalysts can be prepared using different MOF precursors, such as ZIF-67 (with a Co node)[39], ZIF-8 (with a Zn node)[40], core-shell ZIF-8@ZIF-67[41], DUT-58 (Co) MOF[42], enantiotopic chiral 3D MOFs[43, 44], etc. Except for cobalt, other transition metals were also synthesized into TM-N-C, such as Cu-N-C[45] and Fe-N-C[46].

In fact, the activity of TM-N-C composites catalysts depends on not only transition metal-nitrogen sites but also the electronic structure of carbon, which can be optimized by modifying the transition metal core. Transition metal alloys such as NiFe alloy[47], CoFe alloy[48], FeCu alloy[49], ZnCo alloy[50], etc, have been developed for ORR and OER bifunctional electrocatalysts. Single

transition metal atom catalysts usually exhibit promising activity towards oxygen reactions for the single-atom metal can provide improved active sites in the aspects of quantity and quality. In the past ten years, extensive investigations have focused on designing single-atom electrocatalyst even though it's difficult to precisely control the synthesis process and characterize the single-atom active sites.

2.3.2. Carbon-Based Transition Metal Compounds

Although TM-N-C composites electrocatalysts are promising ORR catalysts, as illustrated in Figure 4, they always suffer from high OER overpotential. To design high-efficiency bifunctional catalysts requires further improvement of the OER activity. Carbon-based transition metal compounds including metal oxides, metal hydroxides, metal phosphides, metal nitrides, metal sulfides, and metal carbides have been developed. Figure 5 shows the strategies for gaining carbon-based transition metal compound materials from metal-organic framework precursors.

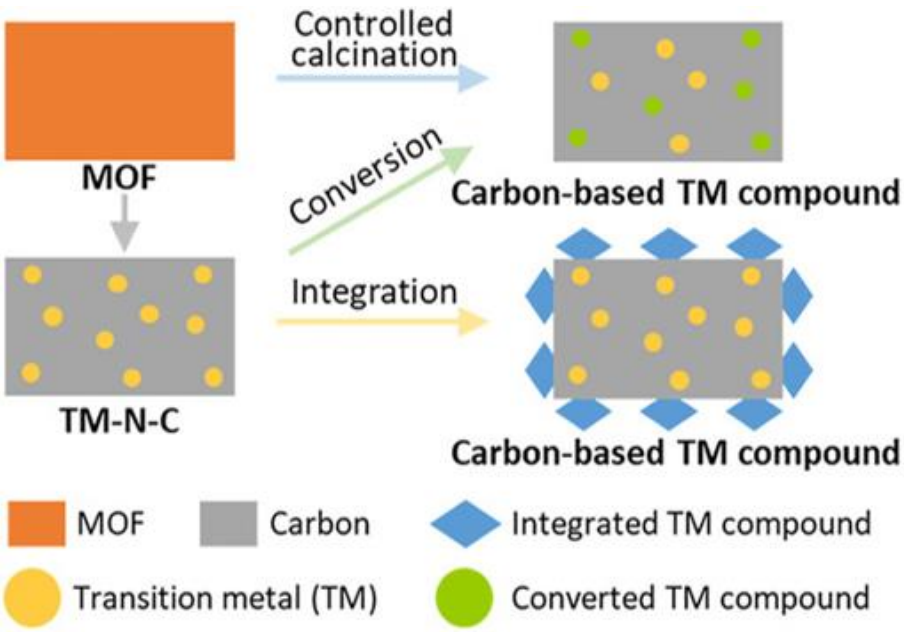

Figure 5: Strategies for gaining MOF-derived carbon-based transition metal compound[2]

The first way is to directly obtain carbon-based transition metal compound materials from the calcination of MOF precursors[51, 52]. The second method is to convert or partially transfer the metal particles by well-conditioned thermal reactions[53-55]. Another method is to generate metal compounds through coating, depositing, or other integration methodologies[11, 56, 57].

2.3.3. Metal-free Carbon Catalysts

Comparing with the previous two types of MOF-derived electrocatalysts, more studies on the bifunctionality of metal-free carbons are still required. Some pioneering investigations on this catalyst materials provide valuable experience for its further development. Usually, the metal-free carbon materials are obtained by the high-temperature sintering process and then leaving N-doped

carbon frameworks with highly-dispersed pores as well as extremely high surface areas. For this strategy, ZIF-8 is the most popular precursor for Zn intermediates are likely to evaporate under high temperature[58]. Metal-free carbon catalyst is a sort of promising ORR electrocatalysts, while it suffers from insufficient OER activity. Other than generating N-C active sites by nitrogen doping, several other heteroatoms have also been introduced such as boron[59] and phosphorus[60], for improving the OER activity of MOF-derived metal-free carbon catalysts.

3. Physical and Electrochemical Characterization Methods

This section introduces the physical and electrochemical characterization techniques which are important tools to help to quantitatively compare samples. The physical characterization methods including transmission electron microscopy (TEM), scanning electron microscopy (SEM), X-Ray diffraction (XRD), X-ray photoelectron spectroscopy (XPS) are used to determine the crystal structure, morphology, and chemical composition. The electrochemical measurement by the three-electrode testing system is used to reveal the thermodynamic and kinetic activities of the as-prepared catalysts towards ORR and OER.

3.1. Scanning Electron Microscopy (SEM)

Scanning electron microscopy is probably one of the most popular and versatile methods

available for viewing the topological features, structure, and atomic compositions by utilizing focused high-energy electrons beam scanning the material surface. SEM can analyze both organic and inorganic samples, which enables its widespread application across various fields (e.g., biology and materials science). Benefiting from the short wavelength of electrons (1.23 nm) and accompanied by electromagnetic condenser lenses, SEM usually can obtain promising magnification (50 X -200000 X) and better resolution (< 1 nm) to reveal the surface morphology of nanomaterials. SEM requires that the scanned material surface must be electronically conductive. For those unconducive samples, conductive nanoparticles like gold and carbon are usually sputtered on the surface of them to fulfill this requirement.

As shown in Figure 6, the operation of SEM uses a beam gun to release electrons serving as an illumination source. And then, the electrons are accelerated up to dozens of keV energy. After that, the high energy electron beams are focused into the electromagnetic lens. The finely focused beams are then injected to the surface of the specimen. Generally, several types of electrons are generated when the electrons hit the specimen surface, revealing various information of the sample. The secondary electrons, produced by the specimen atoms ionization, can be translated into the topography and morphology signals. Backscattered electrons escaping from the material surface usually reveal the composition information by showing different contrasts. During the deexcitation process, another type of electron called Auger electrons is produced by absorbing the released energy, which provides the information associated with the chemical composition of the top few atomic layers of the sample.

Electromagnetic lenses are introduced for the purpose of focusing the spread beams.

Specifically, the electromagnetic lenses are made by coils and wires. The pathway of electron beams is simply adjusted when they are going through the coils with flow current. The first lens is called anode plate which is used to diverge the electron beams. Then two condenser lenses and an aperture are applied for the convergence and collimation of the beams. Besides, the parallel beams are focused into a fine probe on the sample surface by an objective lens with certain demagnification.

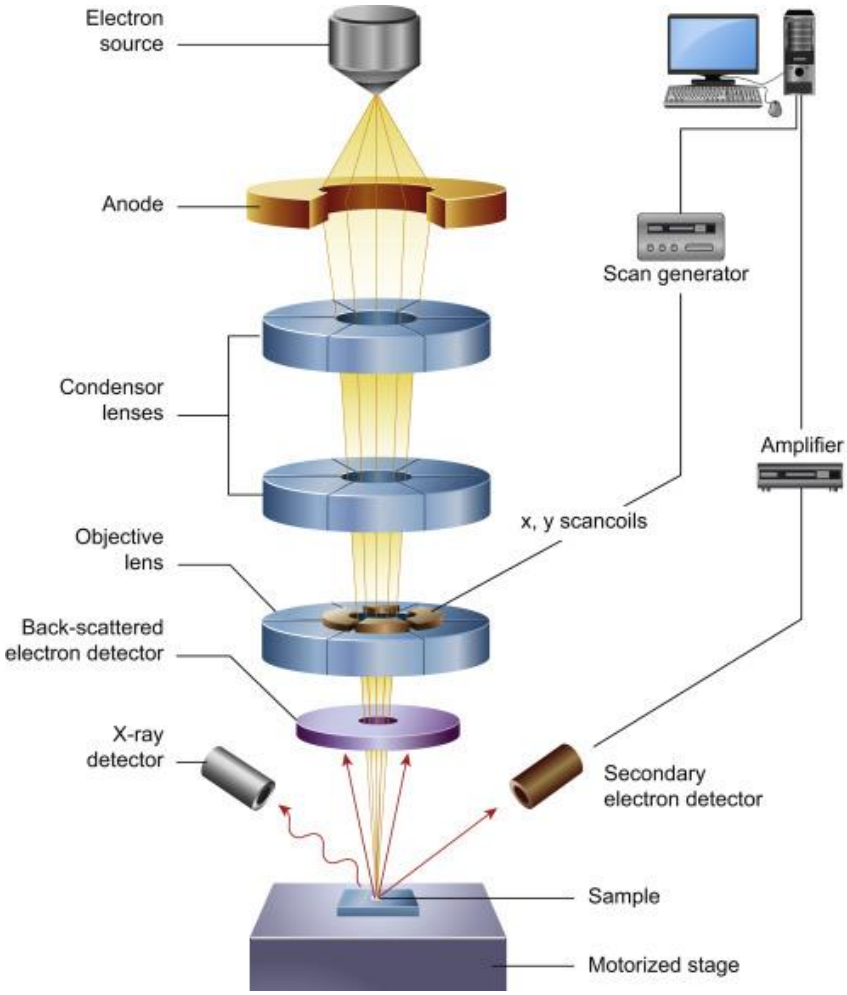

Figure 6: Schematic diagram of a scanning electron microscope (SEM)

3.2. Transmission Electron Microscopy (TEM)

Transmission electron microscopy (TEM) is a microscopy technique with higher resolution (< 1 Å) and higher magnification (500 X -2000000 X) that widely applied to directly investigate materials for imaging their morphological and crystallographic information, such as the crystal lattice structure and atomic-scale defects. Same as SEM, the TEM is usually used in a wide range of various fields such as in-situ reaction investigation, nanotechnology, biology, etc.

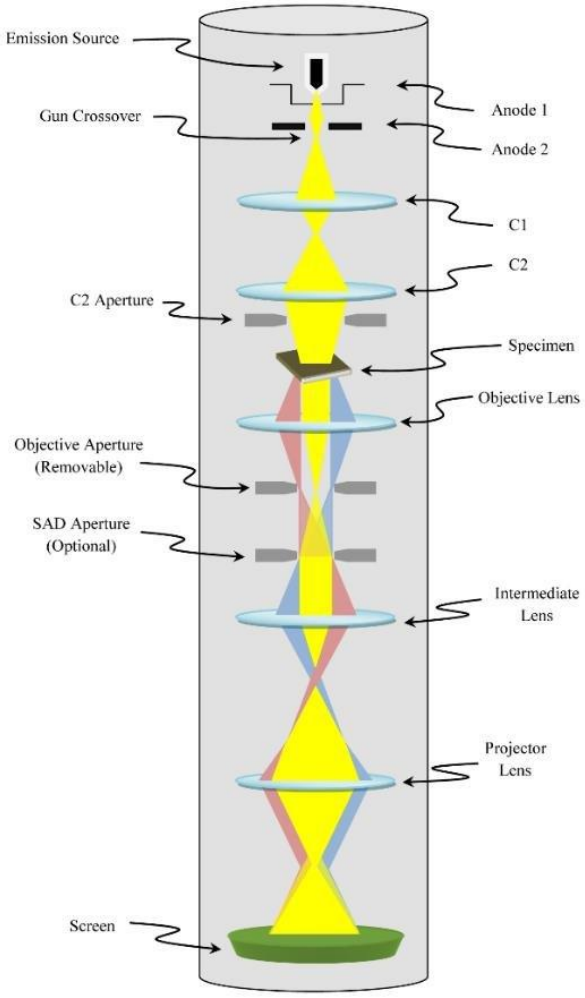

Figure 7: Schematic diagram of a transmission electron microscope (TEM)

Figure 7 presents the components of a TEM which can be mainly classified into three parts. Viewing from the top, the condenser lens system consists of an electron gun, two condenser lenses, and an aperture. The electrons are emitted from the electron gun through Schottky, thermionic, or field emission. The condenser system determines the illumination of the specimen by controlling the aperture. Specifically, the electron beams transmit through the specimen after being focused by those electromagnetic lenses. The second part is called the imaging system which is composed of an objective lens, an objective aperture, a selected area diffraction aperture, an intermediate lens, a projector lens, as well as an observation system for the images and diffraction pattern. The distributed electrons finally hit on a fluorescent screen which will display an image through a photographic emulsion. Moreover, for modern technology, a digital camera is usually installed in TEM instruments to record he obtained images followed with the analysis by PCs. Last but not least, to keep the chamber clean and generate controllable electron beams, a vacuum system is always needed. Typical, the specimen must be less than 100 nm thick and prepared on an ultra-thin Cu grid. During the operation, as the electron beams are interacting with the specimen atoms, simultaneously undergoing elastic and inelastic scattering.

Besides imaging characterizations and atomic morphology of the material's surface, the chemical composition can be obtained by applying the energy-loss spectrum of electron-energy-loss spectroscopy (EELS), and the crystal structures coupled with lattice parameters can be observed by the selected area electron diffraction (SAED), respectively.

3.3. X-ray Diffraction (XRD)

XRD is a popular technique that is used to investigate crystal structures and chemical components of the materials. The basic operation principle is to utilize the feature that X-ray can be diffracted in the crystal lattice to generate an interference pattern. And then the intensities of those patterns will be detected and collected as the information of the lattice planes. Basically, the XRD consists of three elements: an X-ray tube, a sample holder, and an X-ray detector. The X-ray source of XRD is usually copper and molybdenum. As shown in Figure 8, the detector and X-ray tube rotate together, or only X-ray tube moves. When the X-ray tube irradiates with a certain incident angle, the corresponding diffraction angles are detected. Therefore, the information of the lattice is related to both incident position and intensity.

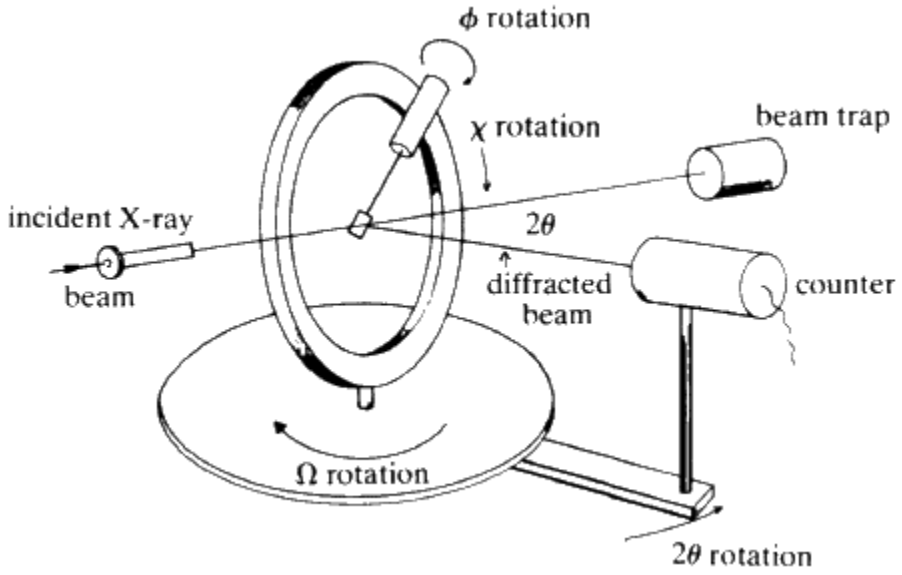

Figure 8: Schematic diagram of XRD layout

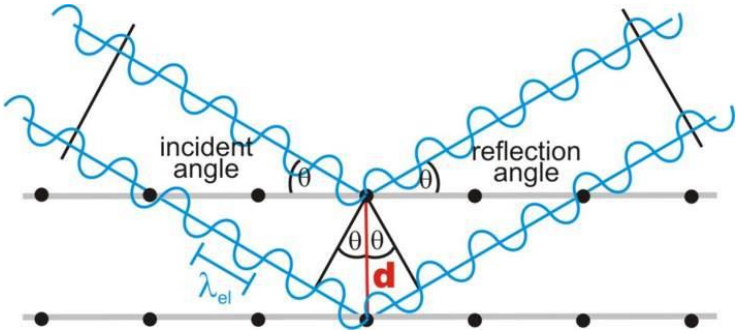

Figure 9: Operational diagram of Bragg's Law

Bragg's law is always used to relate the lattice spacing and X-ray incident angles, which is presented in the following well-known brief equation:

$$2dsin\theta = n\lambda \tag{23}$$

in which: d is lattice spacing, θ stands for the X-ray incident angle (half of the peak position), n is an integer, and λ represents X-ray wavelength.

Furthermore, from the XRD patterns, the grain size of the sample powder can be deduced from the Debye-Scherrer equation which is given below:

$$\tau = \frac{k\lambda}{\beta cos\theta} \tag{24}$$

where: τ is the mean size of the ordered crystalline, k is a shape factor, β is line broadening at half of the maximum intensity of the peak, θ stands for the X-ray incident angle (half of the peak position), and λ represents X-ray wavelength.

3.4. X-ray Photoelectron Spectroscopy (XPS)

XPS is a method that provides information on the elemental composition, empirical formula, electronic structure of atoms, chemical and electronic states of the certain elements exist in a material. What's more, except for showing what elements exist within a film, it also demonstrates what elements they are bonded to.

The basic principle of XPS is mainly related to energy conservation. X-rays are firstly generated and hit the sample, resulting ejected electrons are captured by the detectors and analyzers to form XPS signals. The schematic of the XPS setup is shown in Figure 10. Especially, the total energy introducing to the system is equal to the X-ray's energy before bombarding at the sample, which can be calculated by the known wavelength. After interacting with the sample atoms, electrons will be released from the sample with new kinetic energy according to the photoelectric effect. As a result, it's easy to obtain the amount of energy that is absorbed by the atoms of the sample. The resulted absorbed energy value represents the binding energy (also called ionization energy) of the atom, The binding energy tells us the orbitals from which those electrons are activated and emitted and the information of the chemical bonds. What's more, the electrons configurations and fingerprints for atoms of the material can be obtained due to distinct binding energies of different electron shells.

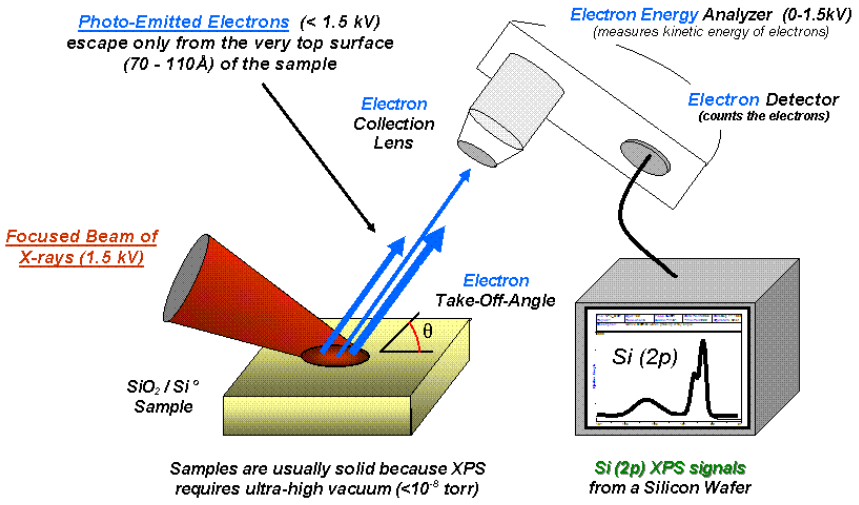

Figure 10: Basic components of an XPS system

3.5. Electrochemical Measurements

To evaluate the electrochemical performance of the as-prepared catalysts, a serious of tests were carried out in a three-electrode system.

Voltammetry experiments are used in analytical chemistry by measuring the current as the potential is varied. To carry out such an experiment, one requires at least two electrodes. The first one is a working electrode, which applies a certain desired potential and manages to generate charges transfer from and to the catalyst material on it. The other electrode is an auxiliary electrode which plays the role of supplying electrons as well as a reference potential to the working electrode. However, this two-electrode system has some disadvantages. One of the most serious problems is that for a single electrode, it's hard to maintain a constant and stable potential while passing current to counter the redox reactions occurring at the working electrode. The three-electrode system

provides a possible way to solve this issue. A reference electrode and a counter are introduced into the system for the functions of providing a reference potential versus working electrode and supplying electrons, respectively. For the reference electrode, without current passing by, it only serves as a reference in measuring the working electrode's potential. On the other hand, all the current required to balance the current occurring at the working electrode during the redox reactions passes through the counter electrode. The three-electrode system is usually designed as a rotating disk electrode (RDE), which is shown in Figure 11.

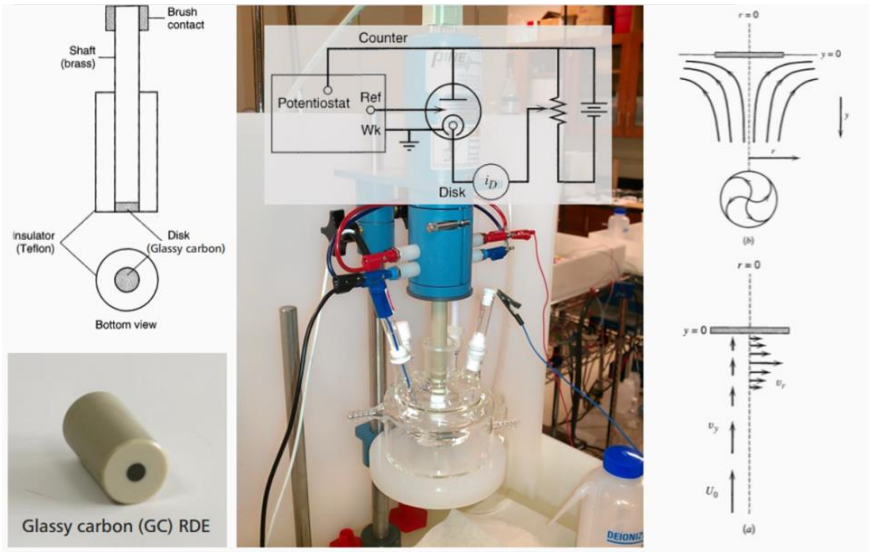

Figure 11: Three-electrode system setup

All the electrochemical characterization results are gained by applying linear sweep voltammetry tests in RDE. Linear sweep voltammetry is one of the most popular voltammetric methods to evaluate the catalytic activities towards ORR and OER, where the working electrode current is measured and the potential between the reference and working electrodes is swept linearly with time. As the potential is applied to the working electrode, the molecules on the surface

of the electrode are oxidized or reduced and then travel away to let new molecules come and contact with the material surface. At the same time, the electrons flow in or out of the electrode generate a current which directly evaluates the electrons exchange rates via the electrode-electrolyte interface. When the kinetic current becomes higher than the diffusion rate of oxidizing or reducing species between electrolyte and electrode surface, the current reaches a plateau. Taking ORR as an example, Figure 3 shows an LSV result of ORR of a certain catalyst. As described before, from LSV data, we can evaluate the thermodynamic and kinetic performances of the catalysts by half-wave potential, onset potential, diffusion-limiting current density, K-L plot, Tafel slope, etc.

During the operation process, the rotation of the electrode aims to keep the dynamic stability of the oxygen concentration on the electrode surface. The electrode reactions consist of five elementary steps: mass transfer, adsorption, surface reaction, desorption, and mass transfer. Oxygen reduced extremely fast on the electrode surface, which means the oxygen concentration close to the electrode surface drop fast. When oxygen is enough, the current is controlled by reaction dynamics, where the Faradic current (current induced by redox reactions) increases with the enlarging of overpotential. On the other hand, when the oxygen concentration on the electrode surface isn't high enough, the Faradic current won't increase with larger overpotential, and the reaction current is mainly determined by the oxygen transfer process. Thus, the electrode rotation speed determines the thickness of the diffusion layer on the electrode surface, where oxygen concentration keeps dynamic stability. The higher of the speed, the larger amount of oxygen moving from the bulk electrolyte to the electrode surface, thus, more abundant reactants and larger

reaction current.

4. Experiment and Characterization

Of various types of methods used to mitigate the oxygen reaction overpotential, MOF-derived metal oxide and metal phosphides have shown great promise. Some researches have demonstrated that cobalt phosphide has a good OER activity[61, 62]. While on the aspect of ORR activity, it has been reported the highly exposed (211) crystal face of CoP makes it an efficient catalyst[63]. However, in general, cobalt phosphides are lacking activities towards ORR than other efficient electrocatalysts. Up to now, a lot of works have been done to illustrate the outstanding ORR activity of cobalt oxide[64, 65]. However, its OER activity is rather insufficient for poor electronic conductivity and structural stability[66]. Zhu's group revealed that the conjugate interface between CoP and CoO result in the redistribution effect of electrons, promotes the adsorption of OH^- anions, and thus synergistically optimizes Gibbs free energies for the OER process[15]. At the same time, the interdoping effect of O-P bond between the interface improves the electron transfer, thus enhances the ORR activity.

The purpose of this work is to design a promising bifunctional electrocatalyst for ORR and OER. In this section, Co-HMT-derived CoO/Co_xP heterostructured nanoparticles catalyst is demonstrated, as well as three contrast samples including pure CoO nanoparticles, Co_xP nanoparticles, and physically mixed CoO+Co_xP catalyst. Particularly, the CoO/Co_xP

heterostructured nanoparticles catalyst can achieve better bifunctionality than other samples including benchmark Pt/Ir catalyst.

4.1. Preparation of the CoO/Co_xP heterostructured nanoparticles

Typically, 2.07g cobalt nitrate ($Co(NO_3)_2 \cdot 6H_2O$) and 1g hexamine (HMT: $C_6H_{12}N_4$) with a molar ratio of 1:1 were dissolved in 30ml and 50ml absolute ethanol separately. The next step was to add the former solution dropwise into another one under vigorous stirring. We also investigate the effect of $Co(NO_3)_2$/HMT molar ratio on the final morphology of the product, where we only changed the adding amount of $Co(NO_3)_2 \cdot 6H_2O$ with the quantities of HMT and ethanol kept constant. Upon the solutions were mixed, the pink precipitate was immediately generated, which demonstrated the formation of Co-HMT nanosheets. The mixed solution was further kept stirring for 12 h for full reaction. After that, the designated Co-HMT bulk crystal was gained by vacuum filtration and washed by ethanol for several times to remove unreactive species, and then dried at 80℃ overnight in a vacuum oven.

Sodium hypophosphite ($NaPH_2O_2$) was selected as the P source for the subsequent phosphorization process. Specifically, the Co-HMT nanosheets and $NaPH_2O_2$ were mixed with a certain ratio (Co/P=1:10), and then directly calcinated at 400℃ for 2 h in an Ar atmosphere at a heating rate of 5℃ min^{-1}. The obtained final products were designated CoO/Co_xP. The schematic of the synthesis procedure is illustrated in Figure 12a and b.

Step 1: Dissolve and mix the metal salt and organic ligand into ethanol and stir for 12h, then obtain the precursor by vacuum filtration, finally dry at 80℃ overnight in a vacuum oven.

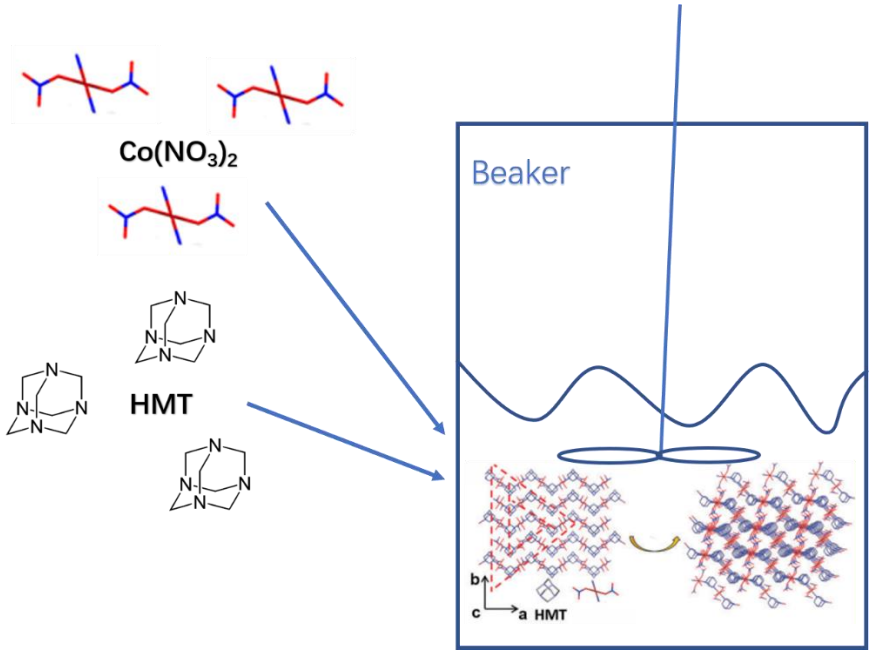

Figure 12: Schematic of the preparation of Co-HMT precursor

Step 2: Calcinate the precursor with $NaPH_2O_2$ at 400℃ for 2 h in an Ar atmosphere at a heating rate of 5℃ min^{-1}

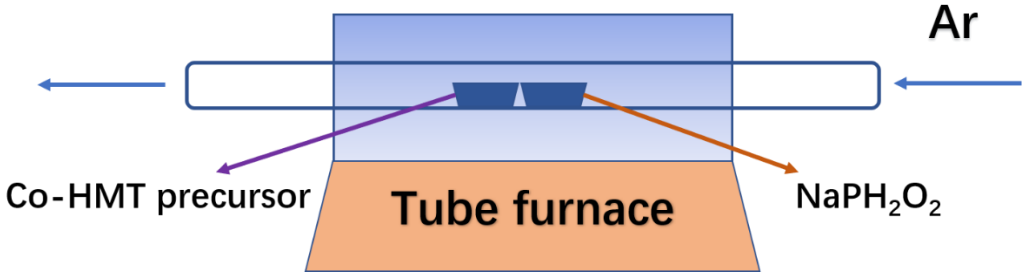

Figure 13: Schematic of the preparation of CoO/Co_xP catalyst

4.2. Materials Characterization

The microscopic morphology and structure of the as-prepared catalyst materials were carried out by transmission electron microscopy (TEM, JEOL 2010F) and scanning electron microscopy (UltraPlus FESEMs (with EDX/OIM); FEI Quanta Feg 250 ESEM (with EDX)). X-Ray Diffraction (A Rigaku MiniFlex 600 X-ray diffractometer with the source of a Cu Kα irradiation) was applied to study the crystal structures. X-ray photoelectron spectroscopy (XPS) data was collected by a Thermal Scientific K-Alpha spectrometer to investigate the surface chemical environment of the samples. A Gaussian-Lorentzian mix is used for analyzing XPS peaks. "Shirley" type background was selected as the background while analyzing. Meanwhile, the binding energy scale was calibrated to fix the C sp^3 peak at 284.8eV[67].

4.3. Electrochemical Performance Measurement

The electrochemical performance of as-prepared catalysts on ORR and OER was carried out on an electrochemical workstation (Biologic VSP 300). The oxygen reactions were measured in a three-electrode glass cell system in 0.1M KOH solution under standard pressure and temperature. A saturated calomel electrode (SCE) and graphite rod were used as the reference and counter electrodes, respectively. The working electrode is a glassy carbon rotating disk electrode (RDE) with an effective surface area of 0.196 cm^{-2}. All of the tested results were finally calibrated to the reversible hydrogen electrode (RHE) based on the Nernst equation:

$$E_{RHE} = E_{SCE} + 0.241 + 0.059 \times pH \quad (25)$$

To obtain a homogeneous catalyst ink, 5mg of the as-developed catalyst was dispersed into the 1000μL solution consisting of 960μL ethanol and 40μL Nafion, followed by ultrasonication for 30min. Then, 21μL of the as-prepared ink was pipetted dropwise on the glassy carbon surface to achieve a loading of 0.53mg cm^{-2}. Commercial precious Pt/C (28wt.% Pt) and Ir/C (20wt.% Ir) catalysts were used as the benchmark references and prepared according to the same procedure. The measurement was conducted by linear sweep voltammetry (LSV) from -1 to 0 V (versus SCE) for ORR and from -0.1 to 0.8 V (versus SCE) for OER with the scan rate of 5 mV s^{-1} and a rotating speed of 1600 rpm. During the process of testing, O_2 or N_2 was always purged into 0.1M KOH solution for 30min before ORR or OER measurements, respectively. Furthermore, a series of LSV at a scan rate of 5 mV s^{-1} with the rotating speed ranging from 400 rpm to 1600 rpm were carried out to study the kinetics of the as-synthesized and commercial catalysts. All the measured polarization curves were calibrated by IR compensation in the alkaline electrolyte. The electron-transfer number per molecule is calculated based on the Koutechy-Levich (K-L) equation:

$$\frac{1}{J} = \frac{1}{J_L} + \frac{1}{J_K} = \frac{1}{B\omega^{1/2}} + \frac{1}{J_K} \quad (26)$$

$$\mathrm{B} = 0.62\mathrm{nF}C_0(D_0)^{2/3}\upsilon^{-1/6} \quad (27)$$

where: J is the measured current density; J_K is the kinetic current density; JL is the diffusion-limiting current density; B is Levich slope; ω is the rotating speed (rad s^{-1}); n is electron transfer number; F stands for Faraday constant (96485 C mol^{-1}); C_0 (1.2×10^{-3} mol L^{-1}) is the bulk concentration of oxygen; D_0 (1.9×10^{-5} cm^2 s^{-1}) is the diffusion coefficient of oxygen; v (0.01 cm^2 s^{-1}) refers to the kinetic viscosity of the electrolyte.

4.4. Results and Discussion

The brief and general synthesis strategy of heterostructured CoO/Co_xP nanoparticles is demonstrated in Figure 12. Overall, the preparation process can be divided into two steps, which involves the synthesis of Cobalt-hexamine (Co-HMT) as the precursor via a wet chemistry method and a subsequent low-temperature annealing process. Herein, we take CoO/Co_xP as an example to illustrate these processes. Firstly, the pink precipitation of Co-HMT nanosheets can be immediately generated by the mixing of $Co(NO_3)_2$ and HMT with a molar ratio of 1:1 in anhydrous ethanol. According to the previous research, from the coordination chemistry point of view, the HMT molecule serves as bridging ligand to connect transition metal ions through chemical coordination to form MOFs with different morphologies[68].

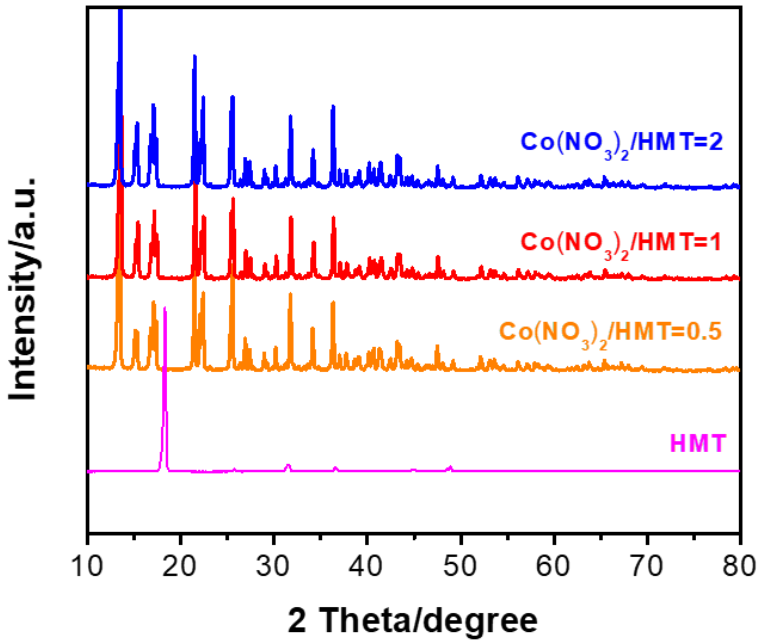

Figure 14: XRD pattern of Co-HMT with molar ratios of 0.5, 1, 2 and the pristine HMT.

In Figure 14, the powder X-ray diffraction (XRD) patterns of Co-HMT MOFs with a series of $Co(NO_3)_2$/HMT molar ratios as well as pristine HMT were measured. The notable diffraction differences between Co-HMT and pure HMT indicate that Co-HMT is successfully synthesized by the coordination of Co species and HMT ligands. In fact, the as-synthesized bulk crystal is the stack of Co-HMT layer by layer. Based on the previous researches from other groups, in the Co-HMT MOFs, a supermolecular chain of $[Co(NO_3)_2(HMT)(H_2O)_2]_n$ is formed[69]. At the same time, different unit chains are connecting through ubiquitous hydrogen bonds of OH…N and OH…O[70], resulting in the bulk-like Co-HMT nanosheets.

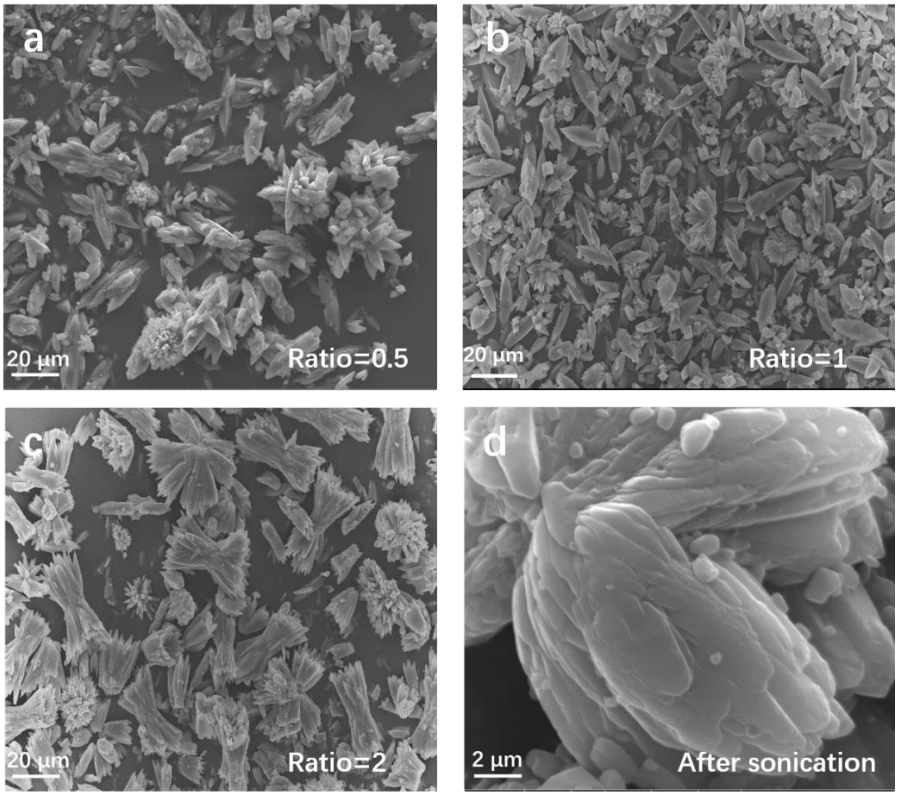

Figure 15: SEM images of Co-HMT with molar ratios of (a)0.5, (b)1, (c)2, and (d) the structure after sonication treatment

Further investigation of the structure of the as-prepared bulk-like Co-HMT nanosheet is

obtained by the scanning electron microscopy (SEM). The Co-HMT framework presents a spindle-shaped bulk morphology (Figure 15 (a), (b), (c)), some of the bulks even stack into the flower-like stack, which may occur due to the hydrogen bonding interactions. In order to prove the spindle-shaped bulks are stacked layer by layer, the Co-HMT sample is exfoliated by sonication in ethanol for 10 minutes. The resultant shows a multilevel structure (Figure 15 (d)) as expected because of the weak hydrogen bonds.

The second step is to convert the Co-HMT bulk frameworks into CoO/Co_xP composite nanoparticles through a direct low-temperature (400℃) phosphating process at a high temperature increasing rate (5℃/min). During the pyrolysis, the HMT ligands serve as a rich nitrogen source, while sodium hypophosphite acts as a phosphorus source. Other than that, the HMT plays the role of reductant reducing the Co^{2+} species to Co nanoparticles, thus resulting in CoO, CoP and Co_2P nanoparticles. As reported by other work before, a huge amount of reducing gases of NH_3, CH_2O and NO are sharply released during the fast phosphorization process[68]. The sharply escaping gases then break the connections between layers and generate a large number of pores with various diameters. Besides, these escaping gases, as well as PH_3 which comes from the decomposition of sodium hypophosphite, make it possible to reduce cobalt ions into cobalt nanoparticles directly under rather a low temperature of phosphorization. Herein, to prove the existence of simple substance Co metal during the pyrolysis process, Co-HMT phosphorized at 320℃ (designed as Co-HMT-320) was applied. As we can see from XRD patterns (Figure 16), the pattern for Co-HMT-320 has several peaks that can be well indexed to metallic Co (PDF#15-0806), Co_2P (PDF#65-2380) and even some weak peaks of CoO (PDF#48-1719). The metallic Co found in

Co_2P likely originated from a concomitant reduction of cobalt precursor species in the presence of the well-known reducing agent (NH_3, CH_2O, NO, and PH_3) for metal ions[71-74]. The peaks of Co appearing at the XRD pattern verify the reducing effect of HMT transferring Co^{2+} species into Co during the low-temperature pyrolysis.

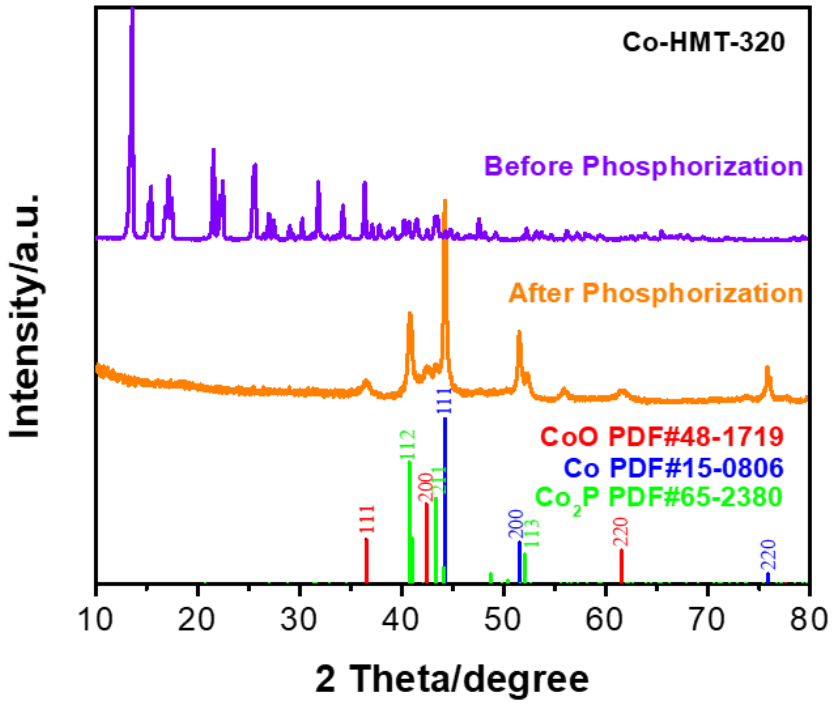

Figure 16: XRD pattern of Co-HMT phosphorized at 320℃.

The XRD diffraction patterns (figure 17) of Co-HMT-400 before and after phosphorization demonstrate the formation of CoO, Co_2P, and CoP nanoparticles. Apparently, complex diffraction peaks between 5° and 30° disappear after the process of phosphorization, indicating the formation of ordered crystalline phases. As revealed in Figure 17, the distinct characteristic peaks at 36.50°, 42.40°, and 61.52° were attributed to the (111), (200), and (220) crystal faces of CoO (PDF#43-

1004). On the other hand, the phosphorized product of CoP presented the characteristic diffraction peaks at 31.60°, 46.23°, and 48.13°, corresponding to (011), (112), and (211) planes of CoP (PDF#29-0497). Beyond that, characteristic diffraction peaks at 40.72° was also detected, which is indexed to the (112) crystal face of Co_2P (PDF#65-2380). Here for clarity, the detected CoP and Co_2P are denoted as Co_xP[15, 75]. Thus the sample can be designated as CoO/Co_xP. The transmission electron microscopy (TEM) (Figure 17)also revealed those nanoparticles on the nanosheets.

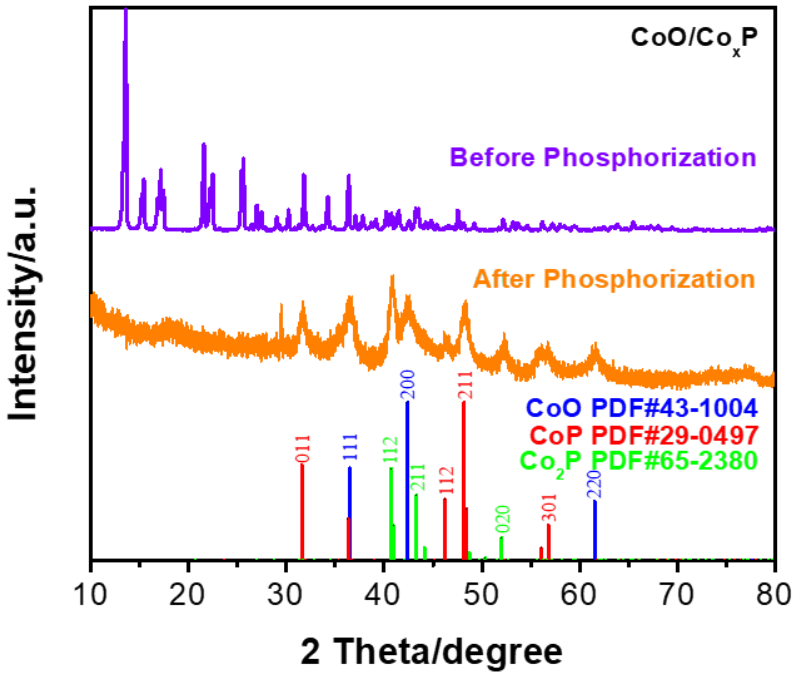

Figure 17: XRD pattern of CoO/Co_xP powders.

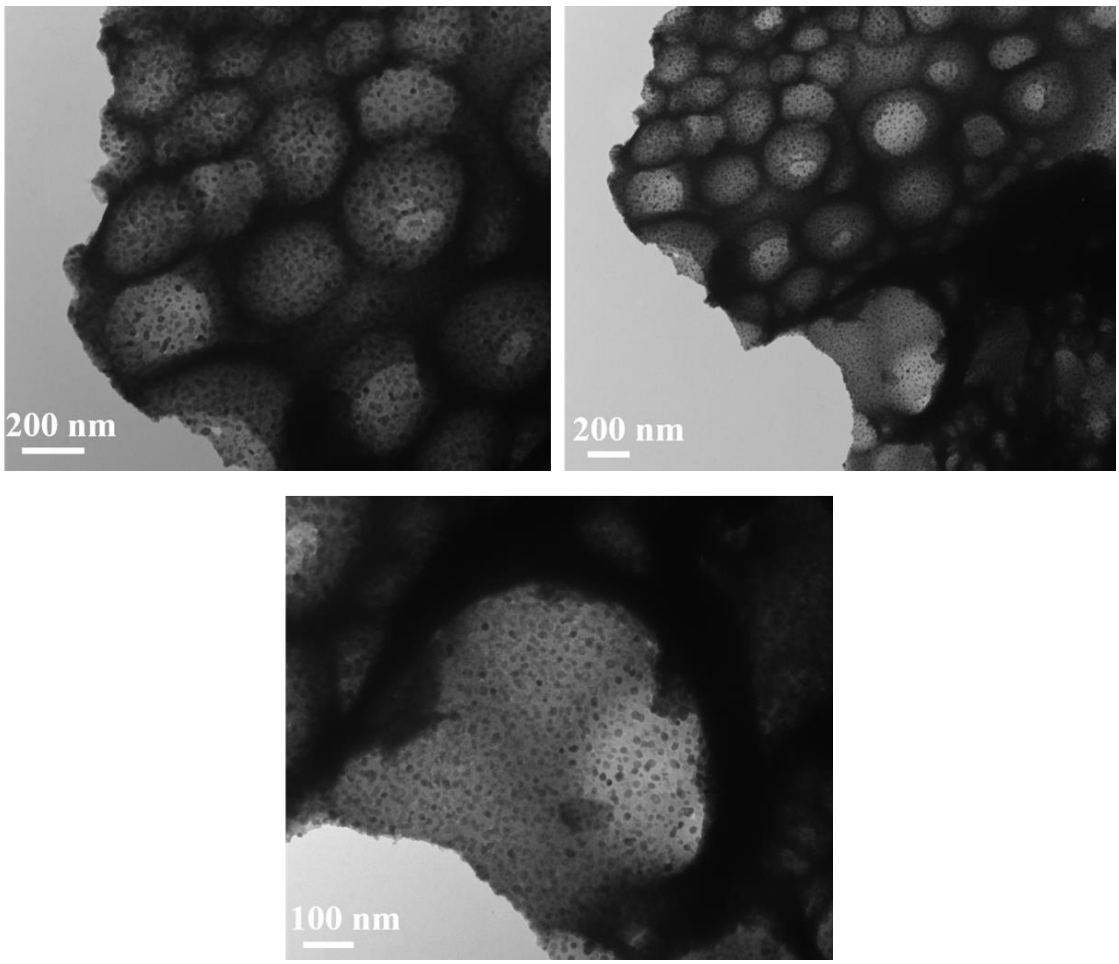

Figure 18: XRD patterns of CoO/Co_xP powders.

As shown in the TEM images in Figure 18, layered material with pores of various diameters was generated during the synthesis process. This morphology may provide large surface area, thus more active sites are exposed. Besides, nanoparticles with the diameters of around 15 nm are finely distributed on the substrate, which also proves the existence of CoO and/or Co_xP nanoparticles. Further evidence of the lattice parameters of these nanoparticles is needed to be measured by HRTEM. Typically, during the low-temperature calcination process, the cobalt atoms dissolved out of the metal-organic framework and were reduced by those escaping gases, leaving a nitrogen-rich framework. It's commonly known that catalysts with large surface area and high pore volume

usually demonstrate satisfactory catalytic activity. Herein, we are investigating the pore distribution conditions of the catalysts by the nitrogen adsorption-desorption method. Besides illustrating the high density of active sites of the as-prepared catalysts by physical characterization, we are doing an experiment to study the ample catalytic sites interface via electrochemical measurement. Unfortunately, these experiments are on the process at present, which can not be presented here.

At the same time, the contrast samples ware successfully synthesized, the pure CoO nanoparticles catalyst was prepared by calcinating Co-HMT precursor without P source, while Co_2P/CoP nanoparticle catalyst was synthesized by phosphorizing Co-HMT at 500℃, the XRD patterns (Figure 19 (a) and (b)) are shown below:

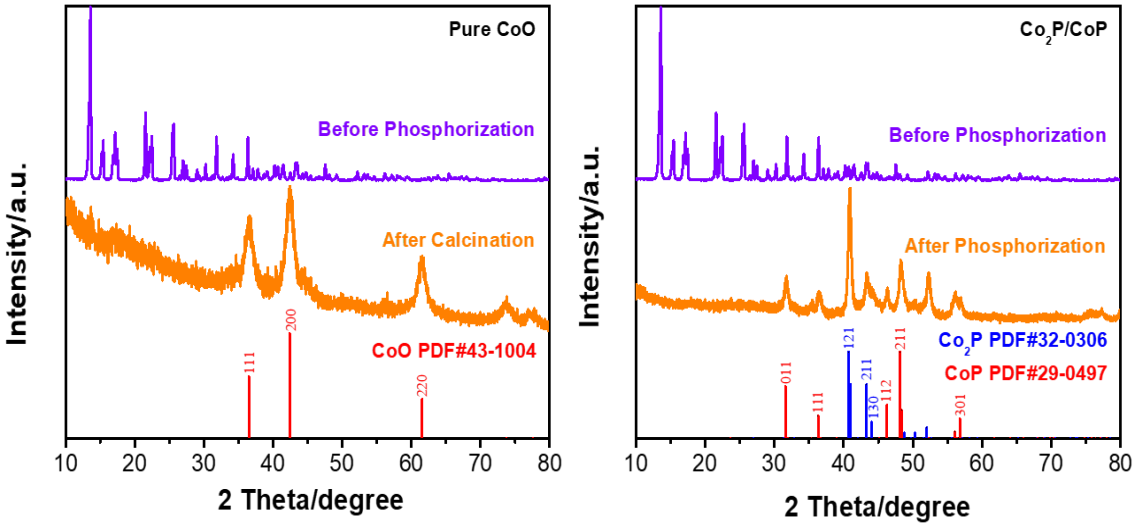

Figure 19: XRD patterns of (a) pure CoO powders, and (b) Co_2P/CoP powders.

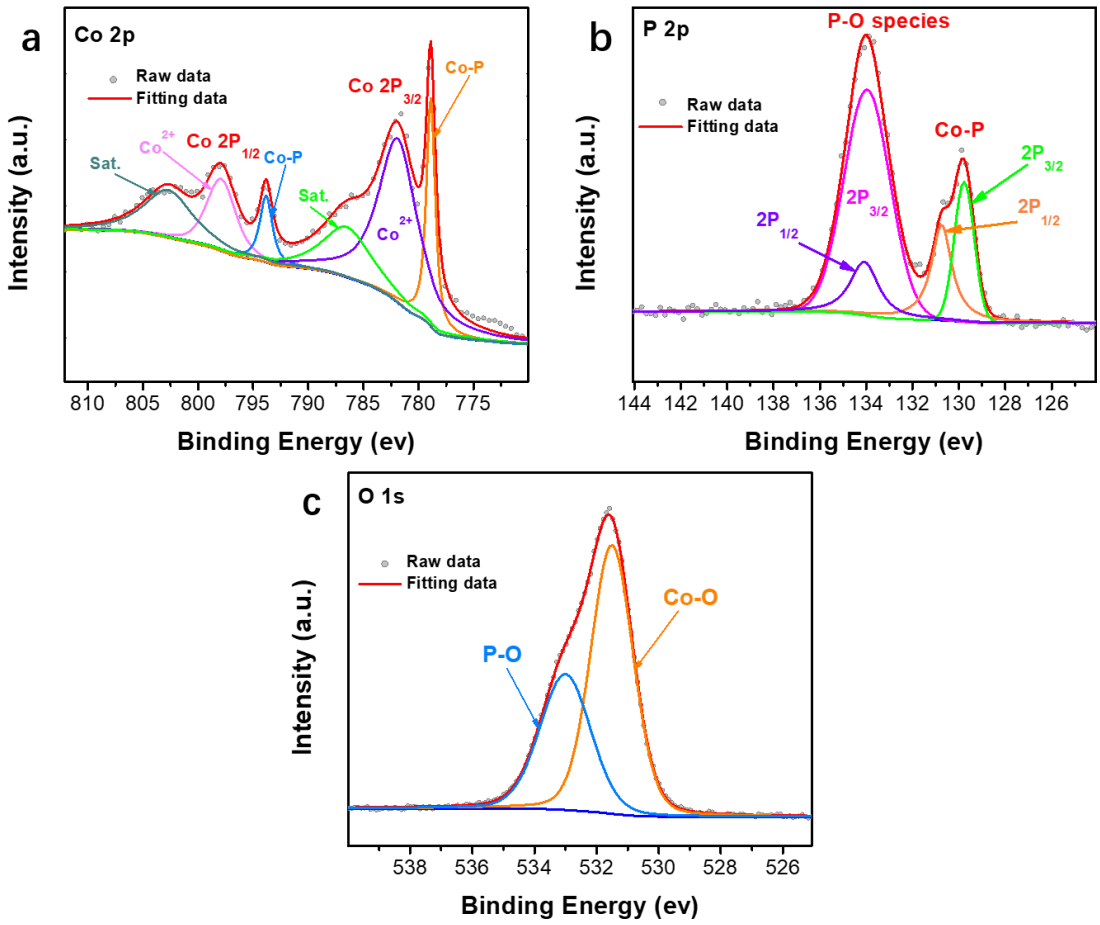

Figure 20: XPS spectra of (a) Co 2p, (b) P 2p, and (c) O 1s for CoO/Co_xP catalyst.

To acquire further insights into the chemical coordination state of the CoO/Co_xP catalyst, XPS analysis was carried out on the product. Figure 20 a-c represent Co 2p, P 2p, and O 1s of the XPS spectrum for the CoO/Co_xP catalyst, respectively. In the high-resolution Co 2p spectra, the peak traced at 778.9, and 781.8 eV are attributed to Co $2p_{3/2}$, while the peak at 786.5 eV represents the satellite peak of Co $2p_{3/2}$. Among them, the peak at 778.9 eV is ascribed to Co-P bond. The peak at 781.8 eV stands for Co^{2+} form of the oxidized Co species, indicating the formation of CoO from metallic Co[76]. The Co $2p_{1/2}$ spectra contains two main peaks at 793.8, 797.9, as well as 802.6 eV,

corresponding to cobalt phosphide, oxidized cobalt species, and satellite peak, respectively[77, 78]. These Co $2p_{2/3}$ and Co $2p_{1/2}$ core peaks including satellite peaks can be attributed to the specific Co-P bond originating from CoP-Co_2P component[79]. Specifically, the binding energy of 778.9 eV is positively shifted compared with that of pristine CoP (778.4 eV), suggesting that the Co_2P species in Co_xP play an essential role in tunning the CoP electronic structure, thus making Co_xP a more effective electron donor. Simultaneously, in the P 2p spectrum, peaks corresponding to P $2p_{3/2}$, and P $2p_{1/2}$ appear at 129.7, and 130.7 eV, respectively. Compared to the simple substance P (130.0 eV), there is a negative shift for the P $2P_{3/2}$ binding energy (129.7 eV), further indicating P atoms take the valence electrons from the Co atoms in Co_xP. Apart from the synergistic effect between CoP and Co_2P species; the electronic interaction also occurred between CoO and Co_xP components during the phosphating process. As exhibited in Figure 20 (c), the peaks present at 531.5 and 533 eV in the O 1s spectra are attributed to Co-O and P-O bonds. Due to the transitional interface formed between the O and P atoms lattice structures, the binding energy of Co-O and P-O slightly shift. Specifically, the binding energy (531.5 eV) of Co-O showed a 0.1 eV negative shift while the peak of Co-P (533 eV) exhibited a positive shift of 0.4 eV[76]. Besides, the binding energy (133.9 eV) of P-O in the P 2p spectra (Figure 18 (b)) also confirms the formation of interface between two phases of CoO and Co_xP species.

Hitherto, the two-dimensional MOF-derived CoO/Co_xP nanoparticles have been successfully prepared. Inspired by the features demonstrated above, the products are believed to have a huge potential as a promising bifunctional electrocatalyst for zinc-air batteries. The ORR and OER activities of the as-prepared CoO/Co_xP were evaluated via linear sweep voltammetry (LSV) in 0.1

M KOH electrolyte. To stick out the morphological and compositional superiority of the heterostructured CoO/Co_xP catalyst, the LSV measurements of pure CoO, Co_xP, and CoO+Co_xP (prepared by mechanically mixing CoO, Co_2P, and CoP nanoparticles) were conducted as well. Furthermore, 28 wt. % Pt/C and 20 wt. % Ir/C commercial catalysts were also measured as the state-of-art benchmarks of ORR and OER, respectively. Overall, the iR-compensated polarization curves of various samples tested at a rotation speed of 1600 rpm are illustrated in Figure 21.

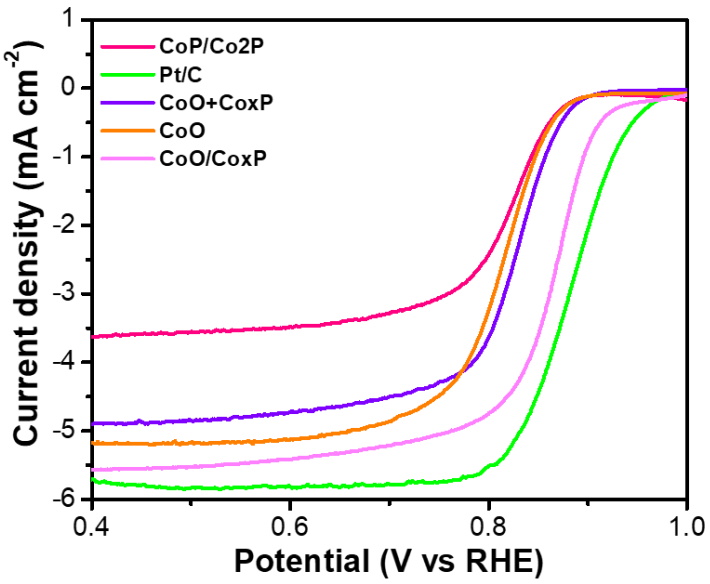

Figure 21: ORR curves of various catalysts in O_2-saturated 0.1 M KOH solution at a rotating speed of 1600 rpm.

Among all the catalysts, pure CoP/Co_2P nanoparticles exhibit the lowest onset potential (E_{onset}) of 0.86V (versus RHE) and smallest diffusion-limited current density of 3.6 mA cm^{-2}. Compared to CoP/Co_2P, CoO nanoparticles show higher E_{onset} and diffusion-limited current density of 0.87 V (versus RHE) and 5.1 mA cm^{-2}, respectively. Similar to CoO, the CoO+Co_xP nanoparticles

demonstrate an onset potential of 0.88 V (versus RHE) and diffusion-limited current density of 4.8 mA cm^{-2}. The increasing E_{onset} and diffusion-limited current density of the latter two catalysts are probably due to the superior ORR activity of CoO to CoP and Co_2P. Benefiting from the ample catalyst/electrolyte interface for active sites originating from high pore volume, as well as the bi-synergetic effect of heterostructured distributed CoO/Co_xP nanoparticles, CoO/Co_xP performs a dramatically improvement on the ORR activity, with a higher onset potential of 0.93 V (versus RHE) and diffusion-limited current density of 5.6 mA cm^{-2}. Although this onset potential still can't keep up with that of commercial Pt/C catalyst (0.98 V versus RHE), CoO/Co_xP exhibits a competitive half-wave potential ($E_{1/2}$) of 0.86 V (versus RHE), which is only 20mV lower than Pt/C but much positive than that of CoO (0.81 V versus RHE), CoP/Co_xP (0.82 V versus RHE), and CoO+Co_xP (0.82 V versus RHE). The fast electrochemical ORR kinetics of CoO/CO_xP is further investigated by the calculated Tafel slopes.

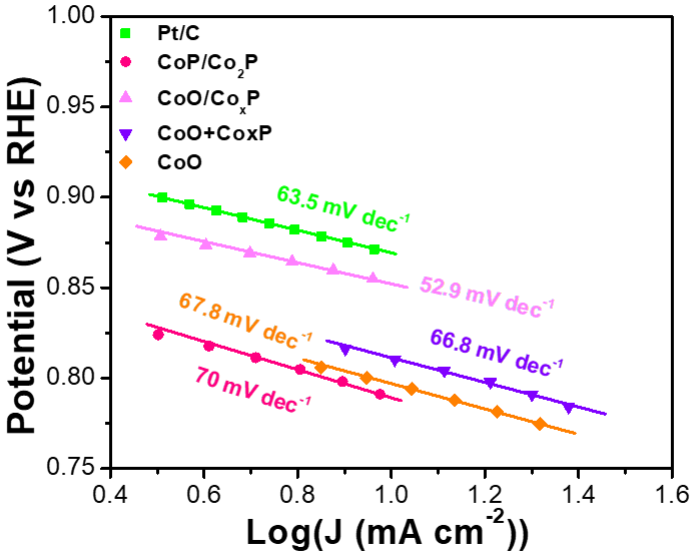

Figure 22: Tafel plots of various catalysts at 1600 rpm in O_2-saturated 0.1 M KOH.

Figure 22 shows that Tafel slopes of CoO/Co_xP (52.9 mV dec^{-1}) is lower than other samples, and even the Pt/C (63.5 mV dec-1), illustrating the fastest ORR kinetics.

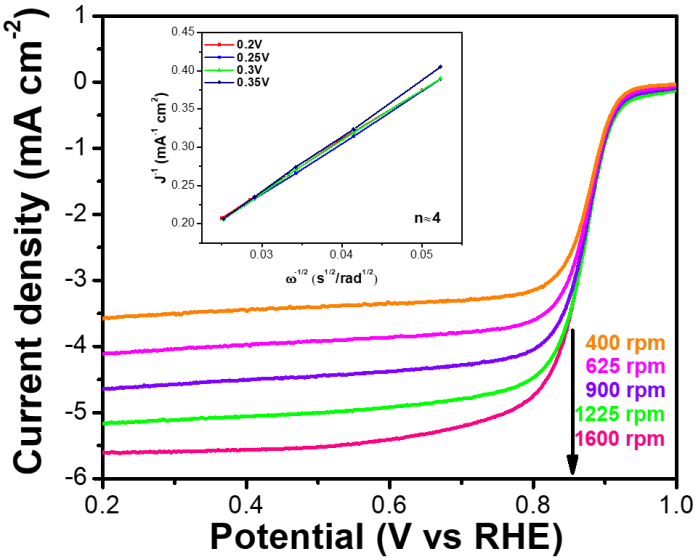

Figure 23: LSV curves of CoO/Co_xP at different rotating speeds (inset: K-L plots obtained under various potentials).

As shown in Figure 23, polarization curves were measured at several rotation speeds ranging from 400 rpm to 1600 rpm. Due to the efficient mass transfer of O_2 from KOH electrolyte to the electrode surface, the limited current densities plateaus uniformly increases as the rotation speed rising. Apart from the ORR activity, the catalytic selectivity is an obbligato factor in judging the catalysts as well. The linearity of the Koutecky-Levich (K-L) plots at different potentials suggest the first-order reaction kinetics about the concentration of dissolved O_2[80, 81]. The electron-transfer number (n ≈ 4) occurring during the ORR process is obtained from the K-L plots, indicating the reaction prefers to reduce O_2 to OH^- directly through a fast four-electron-transfer pathway.

The application of bifunctional electrocatalyst requires not only promising ORR activity but also excellent OER performance. Herein, we also investigated the oxygen evolution activities to confirm the bifunctional property of CoO/Co_xP. Figure 24 illustrates iR-compensated OER LSV curves of all the electrodes in N_2-saturated 0.1 M KOH.

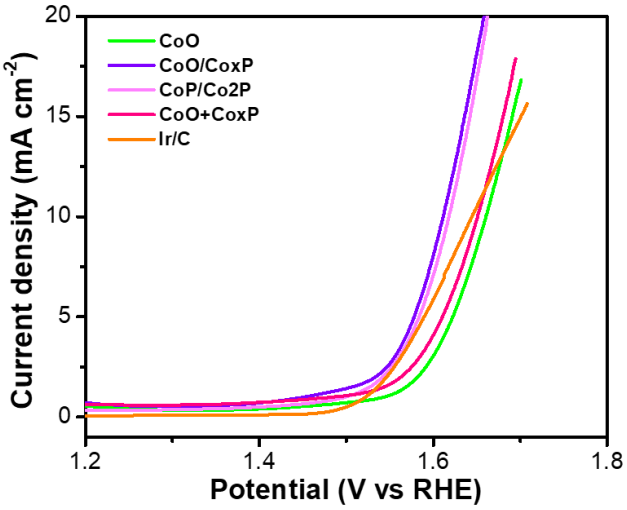

Figure 24: ORR curves of various catalysts in N_2-saturated 0.1 M KOH solution at a rotating speed of 1600 rpm.

The overpotential for OER at a current density of 10 mA cm^{-2} is usually a standard to judge OER activity[82]. Among all the prepared catalysts, CoO/Co_xP shows the lowest potential (1.6 V versus RHE) at the current density of 10 mA cm^{-2}. While for Ir/C, CoO, CoP/Co_2P, and $CoO+Co_xP$ catalysts, the potentials are 1.64 V, 1.66 V, 1.61 V, and 1.65 V, respectively. Specifically, the over-potential of CoO/Co_xP at the current density of 10 mA cm^{-2} is 370 mV, suggesting its superb OER activity. Besides, CoO/Co_xP shows the smallest Tafel slope of 101 mV dec^{-1} relative to the others (Figure 25), revealing the fast OER kinetics on CoO/Co_xP.

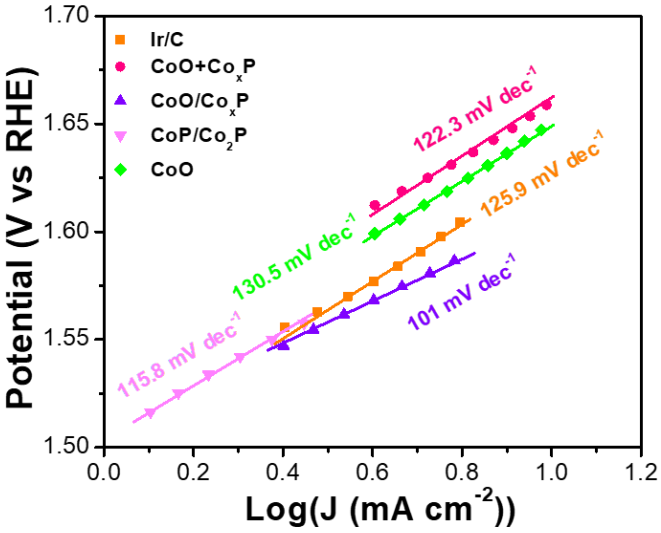

Figure 25: Tafel plots of various catalysts at 1600 rpm in N_2-saturated 0.1 M KOH.

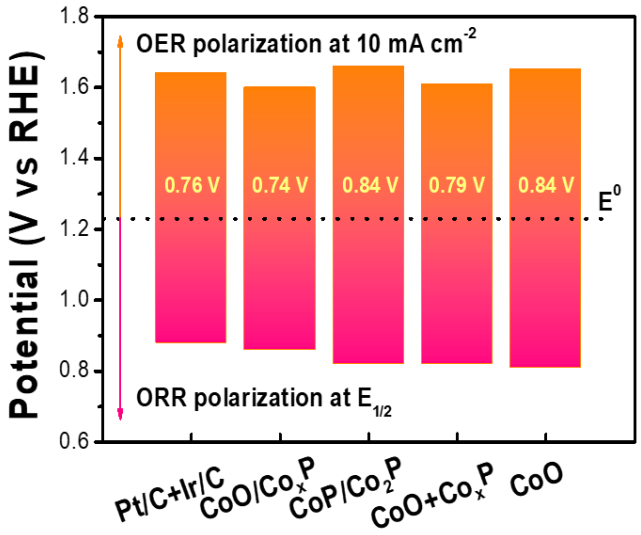

Figure 26: Differences between the ORR $E_{1/2}$ and OER $E_{j=10}$ of different catalysts.

Basing on the above results and analysis, CoO/Co_xP has shown promising electrochemical activities towards ORR and OER. To reveal the bifunctional activity more intuitively, both the ORR half-wave potentials and OER potentials at the current density of 10 mA cm^{-2} are integrated

(Figure 26). The CoO/Co_xP catalyst exhibits the smallest gap (potential difference between ORR $E_{1/2}$ and OER potential at 10 mA cm^{-2}) of 0.74 V among all the as-prepared samples, including commercial Pt/C coupled with Ir/C (0.76 V). Moreover, the horizontal dotted line representing the thermodynamic potential ($E^0(OH^-/O_2)$=1.23 V) serves as a reference to reflect the overpotential regarding ORR and OER.

5. Conclusions of the Thesis and Future Works

5.1. Conclusions of the Thesis

In this thesis, we have designed a CoO/Co_xP heterostructured nanoparticles electrocatalyst by in situ coupling CoO nanoparticles with Co_2P and CoP nanoparticles instead of simply physically mixing them. During the synthesis process, Cobalt(II) nitrate hexahydrate was the transition metal salt, while HMT played the role of organic ligand, a layered Co-HMT framework was prepared as an efficient precursor. The final product was obtained by a following low-temperature phosphorization strategy, during which a huge amount of reducing gases was sharply released to exfoliate the layered structure apart.

XRD, TEM, SEM, and XPS were used to confirm and analyze the morphology and the chemical environment of the catalysts. XRD patterns confirmed the formation of Co-HMT with various molar ratios and illustrated the compositions of as-prepared catalysts. The lamellar structure of the MOF bulk crystal precursor was proved by SEM images. TEM was carried out to

investigate the particles, revealing that the particles with the diameter around 15 nm were uniformly distributed. What's more, viewing from the TEM images, pores with different diameters could be observed. The interaction between CoO and Co_xP nanoparticles and the energy adjusting effect between Co_2P and CoP nanoparticles were revealed by XPS.

In order to study the ORR and OER activities, the electrochemical performances of the as-prepared electrocatalyst were measured in a three-electrode system. The LSV results are summarized in Table 1:

Table 1: Summary of the bifunctional activities of as-prepared catalysts for ORR and OER

	ORR			OER	Bifunctionality
Catalysts	**Onset potential (V)**	**Half-wave potential ($E_{1/2}$, V)**	**Diffusion-limited current density (mA cm^{-2})**	**Potential at 10 mA cm^{-2} ($E_{j=10}$, V)**	$\Delta E = E_{j=10} - E_{1/2}$
Pt/C+Ir/C	0.98	0.88	5.7	1.64	0.76
CoO/Co_xP	0.93	0.86	5.6	1.60	0.74
CoO+Co_xP	0.88	0.82	4.8	1.61	0.79
CoO	0.87	0.81	5.1	1.65	0.84
Co_2P/CoP	0.86	0.82	3.6	1.66	0.84

Note: All potentials presented in this table are demonstrated versus reversible hydrogen electrode (RHE) and obtained in 0.1 M KOH solution using the glassy carbon working electrode.

In summary, CoO/Co_xP displays the smallest potential gap among all these catalysts, demonstrating its promising bifunctionality towards ORR and OER. Specifically, comparing with the pure CoO, Co_2P/CoP, and CoO+Co_xP catalysts, the CoO/Co_xP catalyst has the highest half-wave potential of 0.86 V, the highest diffusion-limiting current density of 5.6 mA cm^{-2}, and the lowest overpotential at 10 mA cm^{-2} for OER. In addition, both ORR (52.9 mV dec^{-1})and OER (101 mV dec^{-1})Tafel slopes of CoO/Co_xP outperform other materials, which show the best kinetic

activity of this catalyst. Furthermore, such desirable low potential difference (0.74 V) and overpotential show competitive catalytic bifunctionality of CoO/Co_xP catalyst when comparing with the most of well-developed bifunctional oxygen electrocatalysts reported in recent years (Table 2).

Table 2: Summary of the ORR and OER activities of recently reported bifunctional electrocatalysts

Catalyst	**ORR: half-wave potential ($E_{1/2}$, V)**	**OER: potential at 10 mA cm^{-2} ($E_{j=10}$, V)**	$\Delta E = E_{j=10} - E_{1/2}$	**Reference**
CoO/Co_xP	0.86	1.60	0.74	This work
CoS_2/SKJ	0.84	1.58	0.74	*ACS Nano* **2019** *13* (6), 7062-7072
$CoO_{0.87}S_{0.13}$/GN	0.83	1.59	0.76	*Adv. Mater.* **2017**, *29*, 1702526
3DOM-Co@TiO_xN_y	0.84	1.62	0.78	*Adv. Mater.* **2019**, *31,* 1806761
Co/Co_3O_4@PGS	0.89	1.58	0.69	*Adv. Energy Mater.* **2018**, *8*, 1702900
CoFe/N-GCT	0.79	1.67	0.88	*Angew. Chem.* **2018**, 130, 16398-16402
Co@Co_3O_4/NC	0.80	1.65	0.85	*Angew. Chem., Int. Ed.* **2016**, *55*, 4087
NC-Co SA	0.87	1.59	0.72	*ACS Catal.* **2018**, *8,* 8961−8969
CoP@CC	0.67	1.68	1.01	*Nanoscale,* **2017**, *9,* 18977
CoP@mNSP-C	0.90	1.64	0.74	*small* **2017***,13,* 1702068
Co_xO_y/NC	0.80	1.66	0.86	*Angew. Chem. Int. Ed.* **2014**, *53*, 8508.

Note: All potentials presented in this table are demonstrated versus reversible hydrogen electrode (RHE) and obtained in 0.1 M KOH solution using the glassy carbon working electrode.

The increase in performance can be attributed to the interpenetrating interfaces between

cobalt oxide and cobalt phosphide, and also the synergistic effect between cobalt phosphides. Meanwhile, the unique morphology originating from the layered Co-HMT framework endow this catalyst with the benefit of abundant catalyst/electrolyte interfaces for catalytic active sites.

5.2. Future works

Although the electrochemical performance of the obtained catalyst is good, further optimization of the ratios of CoO: Co_xP and Co_2P: CoP needs to be done to investigate the influences of the amount of metal oxides and metal phosphides as well as metal content within metal phosphides to the oxygen reaction activity, respectively.

Further results of nitrogen adsorption and desorption and double-layer capacitance measurements are needed to prove the high surface area of the catalyst material and the abundant exposing active sites.

To develop the promising bifunctional electrocatalysts for ORR and OER and applied in the zinc-air battery requires not only great ORR and OER electrochemical activities, but also promising durability and stability. The stability to ORR and OER are usually tested by chronoamperometric (CA) measurement. In addition, the catalyst should be further assembled into zinc-air batteries for the galvanostatic cycling stability test. Other than the stability measurement of the zinc-air batteries, specific capacity, electrochemical impedance spectroscopy, rate capabilities measurement, etc, should also be applied.

References

1. Chi, J.-Q.; Gao, W.-K.; Lin, J.-H.; Dong, B.; Yan, K.-L.; Qin, J.-F.; Liu, B.; Chai, Y.-M.; Liu, C.-G., N, P dual-doped hollow carbon spheres supported MoS2 hybrid electrocatalyst for enhanced hydrogen evolution reaction. *Catalysis Today* **2019,** *330*, 259-267.
2. Zhong, Y.; Xu, X.; Wang, W.; Shao, Z., Recent Advances in Metal-Organic Framework Derivatives as Oxygen Catalysts for Zinc-Air Batteries. **2019,** *2* (4), 272-289.
3. Larcher, D.; Tarascon, J. M., Towards greener and more sustainable batteries for electrical energy storage. *Nature Chemistry* **2014,** *7*, 19.
4. Geng, D.; Ding, N.; Hor, T. S. A.; Chien, S. W.; Liu, Z.; Wuu, D.; Sun, X.; Zong, Y., From Lithium-Oxygen to Lithium-Air Batteries: Challenges and Opportunities. **2016,** *6* (9), 1502164.
5. Li, Y.; Dai, H., Recent advances in zinc–air batteries. *Chemical Society Reviews* **2014,** *43* (15), 5257-5275.
6. Lee, W.; Muhammad, S.; Kim, T.; Kim, H.; Lee, E.; Jeong, M.; Son, S.; Ryou, J.-H.; Yoon, W.-S., Rechargeable Batteries: New Insight into Ni-Rich Layered Structure for Next-Generation Li Rechargeable Batteries (Adv. Energy Mater. 4/2018). **2018,** *8* (4), 1870015.
7. Fu, J.; Cano, Z. P.; Park, M. G.; Yu, A.; Fowler, M.; Chen, Z., Electrically Rechargeable Zinc–Air Batteries: Progress, Challenges, and Perspectives. **2017,** *29* (7), 1604685.
8. Li, Y.; Zhong, C.; Liu, J.; Zeng, X.; Qu, S.; Han, X.; Deng, Y.; Hu, W.; Lu, J., Atomically Thin Mesoporous Co3O4 Layers Strongly Coupled with N-rGO Nanosheets as High-Performance Bifunctional Catalysts for 1D Knittable Zinc–Air Batteries. **2018,** *30* (4), 1703657.
9. Li, Y.; Zhong, C.; Liu, J.; Zeng, X.; Qu, S.; Han, X.; Deng, Y.; Hu, W.; Lu, J., Atomically Thin Mesoporous Co3O4 Layers Strongly Coupled with N-rGO Nanosheets as High-Performance Bifunctional Catalysts for 1D Knittable Zinc–Air Batteries. *Advanced Materials* **2018,** *30* (4), 1703657.
10. Li, S.; Cheng, C.; Zhao, X.; Schmidt, J.; Thomas, A., Active Salt/Silica-Templated 2D Mesoporous FeCo-Nx-Carbon as Bifunctional Oxygen Electrodes for Zinc–Air Batteries. **2018,** *57* (7), 1856-1862.
11. Chen, Y.-N.; Guo, Y.; Cui, H.; Xie, Z.; Zhang, X.; Wei, J.; Zhou, Z., Bifunctional electrocatalysts of MOF-derived Co–N/C on bamboo-like MnO nanowires for high-performance liquid- and solid-state Zn–air batteries. *Journal of Materials Chemistry A* **2018,** *6* (20), 9716-9722.
12. Su, C.-Y.; Cheng, H.; Li, W.; Liu, Z.-Q.; Li, N.; Hou, Z.; Bai, F.-Q.; Zhang, H.-X.; Ma, T.-Y., Atomic Modulation of FeCo–Nitrogen–Carbon Bifunctional Oxygen Electrodes for Rechargeable and Flexible All-Solid-State Zinc–Air Battery. *Advanced Energy Materials* **2017,** *7* (13), 1602420.
13. Wang, M.; Dong, C.-L.; Huang, Y.-C.; Shen, S., Bifunctional cobalt phosphide nanoparticles with convertible surface structure for efficient electrocatalytic water splitting in alkaline solution. *Journal of Catalysis* **2019,** *371*, 262-269.
14. Tao, B. X.; Ye, C.; Li, X. L.; Wang, X. H.; Chen, G.; Li, L. J.; Luo, H. Q.; Li, N. B., Heterogeneous cobalt phosphides nanoparticles anchored on carbon cloth realizing the efficient hydrogen generation reaction. *International Journal of Hydrogen Energy* **2019,** *44* (2), 531-539.
15. Hu, X.; Zhang, S.; Sun, J.; Yu, L.; Qian, X.; Hu, R.; Wang, Y.; Zhao, H.; Zhu, J., 2D Fe-containing cobalt phosphide/cobalt oxide lateral heterostructure with enhanced activity for oxygen evolution reaction. *Nano Energy* **2019,** *56*, 109-117.

16. Chen, D.; Chen, C.; Baiyee, Z. M.; Shao, Z.; Ciucci, F., Nonstoichiometric Oxides as Low-Cost and Highly-Efficient Oxygen Reduction/Evolution Catalysts for Low-Temperature Electrochemical Devices. *Chemical Reviews* **2015,** *115* (18), 9869-9921.

17. Zhang, J.; Wu, X.; Cheong, W.-C.; Chen, W.; Lin, R.; Li, J.; Zheng, L.; Yan, W.; Gu, L.; Chen, C.; Peng, Q.; Wang, D.; Li, Y., Cation vacancy stabilization of single-atomic-site Pt1/Ni(OH)x catalyst for diboration of alkynes and alkenes. *Nature Communications* **2018,** *9* (1), 1002.

18. Zhang, Y.; Ptacin, J. L.; Fischer, E. C.; Aerni, H. R.; Caffaro, C. E.; San Jose, K.; Feldman, A. W.; Turner, C. R.; Romesberg, F. E., A semi-synthetic organism that stores and retrieves increased genetic information. *Nature* **2017,** *551*, 644.

19. Qian, J.; Sun, F.; Qin, L., Hydrothermal synthesis of zeolitic imidazolate framework-67 (ZIF-67) nanocrystals. *Materials Letters* **2012,** *82*, 220-223.

20. Cao, X.; Tan, C.; Sindoro, M.; Zhang, H., Hybrid micro-/nano-structures derived from metal–organic frameworks: preparation and applications in energy storage and conversion. *Chemical Society Reviews* **2017,** *46* (10), 2660-2677.

21. Huang, L.; Zhang, X.; Han, Y.; Wang, Q.; Fang, Y.; Dong, S., In situ synthesis of ultrathin metal–organic framework nanosheets: a new method for 2D metal-based nanoporous carbon electrocatalysts. *Journal of Materials Chemistry A* **2017,** *5* (35), 18610-18617.

22. Xia, W.; Li, J.; Wang, T.; Song, L.; Guo, H.; Gong, H.; Jiang, C.; Gao, B.; He, J., The synergistic effect of Ceria and Co in N-doped leaf-like carbon nanosheets derived from a 2D MOF and their enhanced performance in the oxygen reduction reaction. *Chemical Communications* **2018,** *54* (13), 1623-1626.

23. Wang, Z.-L.; Xu, D.; Xu, J.-J.; Zhang, X.-B., Oxygen electrocatalysts in metal–air batteries: from aqueous to nonaqueous electrolytes. *Chemical Society Reviews* **2014,** *43* (22), 7746-7786.

24. Meng, F.-L.; Liu, K.-H.; Zhang, Y.; Shi, M.-M.; Zhang, X.-B.; Yan, J.-M.; Jiang, Q., Recent Advances toward the Rational Design of Efficient Bifunctional Air Electrodes for Rechargeable Zn–Air Batteries. **2018,** *14* (32), 1703843.

25. Tan, P.; Chen, B.; Xu, H.; Zhang, H.; Cai, W.; Ni, M.; Liu, M.; Shao, Z., Flexible Zn– and Li–air batteries: recent advances, challenges, and future perspectives. *Energy & Environmental Science* **2017,** *10* (10), 2056-2080.

26. Xiao, M.; Zhang, H.; Chen, Y.; Zhu, J.; Gao, L.; Jin, Z.; Ge, J.; Jiang, Z.; Chen, S.; Liu, C.; Xing, W., Identification of binuclear Co2N5 active sites for oxygen reduction reaction with more than one magnitude higher activity than single atom CoN4 site. *Nano Energy* **2018,** *46*, 396-403.

27. Pan, J.; Xu, Y. Y.; Yang, H.; Dong, Z.; Liu, H.; Xia, B. Y., Advanced Architectures and Relatives of Air Electrodes in Zn-Air Batteries. *Adv Sci (Weinh)* **2018,** *5* (4), 1700691-1700691.

28. Suntivich, J.; Gasteiger, H. A.; Yabuuchi, N.; Nakanishi, H.; Goodenough, J. B.; Shao-Horn, Y., Design principles for oxygen-reduction activity on perovskite oxide catalysts for fuel cells and metal–air batteries. *Nature Chemistry* **2011,** *3*, 546.

29. Reda, M.; Hansen, H. A.; Vegge, T., DFT study of stabilization effects on N-doped graphene for ORR catalysis. *Catalysis Today* **2018,** *312*, 118-125.

30. Zhang, Q.; Asthagiri, A., Solvation effects on DFT predictions of ORR activity on metal surfaces. *Catalysis Today* **2019,** *323*, 35-43.

31. Mozurkewich, M.; Benson, S. W., Negative activation energies and curved Arrhenius plots. 1. Theory of reactions over potential wells. *The Journal of Physical Chemistry* **1984,** *88* (25), 6429-6435.

32. Zhang, J.; Xia, Z.; Dai, L., Carbon-Based Electrocatalysts for Advanced Energy Conversion and Storage. *Science*

Advances **2015,** *1*, e1500564-e1500564.

33. Ge, X.; Sumboja, A.; Wuu, D.; An, T.; Li, B.; Goh, F. W. T.; Hor, T. S. A.; Zong, Y.; Liu, Z., Oxygen Reduction in Alkaline Media: From Mechanisms to Recent Advances of Catalysts. *ACS Catalysis* **2015,** *5* (8), 4643-4667.

34. Anjum, M. A. R.; Lee, M. H.; Lee, J. S., Boron- and Nitrogen-Codoped Molybdenum Carbide Nanoparticles Imbedded in a BCN Network as a Bifunctional Electrocatalyst for Hydrogen and Oxygen Evolution Reactions. *ACS Catalysis* **2018**, 8296-8305.

35. Ji, Y.; Dong, H.; Liu, C.; Li, Y., The progress of metal-free catalysts for the oxygen reduction reaction based on theoretical simulations. *Journal of Materials Chemistry A* **2018,** *6* (28), 13489-13508.

36. Man, I. C.; Su, H.-Y.; Calle-Vallejo, F.; Hansen, H. A.; Martínez, J. I.; Inoglu, N. G.; Kitchin, J.; Jaramillo, T. F.; Nørskov, J. K.; Rossmeisl, J., Universality in Oxygen Evolution Electrocatalysis on Oxide Surfaces. **2011,** *3* (7), 1159-1165.

37. Qiu, B.; Cai, L.; Wang, Y.; Lin, Z.; Zuo, Y.; Wang, M.; Chai, Y., Fabrication of Nickel–Cobalt Bimetal Phosphide Nanocages for Enhanced Oxygen Evolution Catalysis. **2018,** *28* (17), 1706008.

38. Xia, B. Y.; Yan, Y.; Li, N.; Wu, H. B.; Lou, X. W.; Wang, X., A metal–organic framework-derived bifunctional oxygen electrocatalyst. *Nature Energy* **2016,** *1*, 15006.

39. Zhang, E.; Xie, Y.; Ci, S.; Jia, J.; Cai, P.; Yi, L.; Wen, Z., Multifunctional high-activity and robust electrocatalyst derived from metal–organic frameworks. *Journal of Materials Chemistry A* **2016,** *4* (44), 17288-17298.

40. Deng, Y.; Chi, B.; Tian, X.; Cui, Z.; Liu, E.; Jia, Q.; Fan, W.; Wang, G.; Dang, D.; Li, M.; Zang, K.; Luo, J.; Hu, Y.; Liao, S.; Sun, X.; Mukerjee, S., g-C3N4 promoted MOF derived hollow carbon nanopolyhedra doped with high density/fraction of single Fe atoms as an ultra-high performance non-precious catalyst towards acidic ORR and PEM fuel cells. *Journal of Materials Chemistry A* **2019,** *7* (9), 5020-5030.

41. Zhang, K.; Guo, W.; Liang, Z.; Zou, R., Metal-organic framework based nanomaterials for electrocatalytic oxygen redox reaction. *Science China Chemistry* **2019,** *62* (4), 417-429.

42. Guo, J.; Gadipelli, S.; Yang, Y.; Li, Z.; Lu, Y.; Brett, D. J. L.; Guo, Z., An efficient carbon-based ORR catalyst from low-temperature etching of ZIF-67 with ultra-small cobalt nanoparticles and high yield. *Journal of Materials Chemistry A* **2019,** *7* (8), 3544-3551.

43. Wang, T.; Kou, Z.; Mu, S.; Liu, J.; He, D.; Amiinu, I. S.; Meng, W.; Zhou, K.; Luo, Z.; Chaemchuen, S.; Verpoort, F., 2D Dual-Metal Zeolitic-Imidazolate-Framework-(ZIF)-Derived Bifunctional Air Electrodes with Ultrahigh Electrochemical Properties for Rechargeable Zinc–Air Batteries. **2018,** *28* (5), 1705048.

44. Zhang, M.; Dai, Q.; Zheng, H.; Chen, M.; Dai, L., Novel MOF-Derived Co@N-C Bifunctional Catalysts for Highly Efficient Zn–Air Batteries and Water Splitting. **2018,** *30* (10), 1705431.

45. Lai, Q.; Zhu, J.; Zhao, Y.; Liang, Y.; He, J.; Chen, J., MOF-Based Metal-Doping-Induced Synthesis of Hierarchical Porous Cu□N/C Oxygen Reduction Electrocatalysts for Zn–Air Batteries. **2017,** *13* (30), 1700740.

46. Xiao, M.; Zhu, J.; Ma, L.; Jin, Z.; Ge, J.; Deng, X.; Hou, Y.; He, Q.; Li, J.; Jia, Q.; Mukerjee, S.; Yang, R.; Jiang, Z.; Su, D.; Liu, C.; Xing, W., Microporous Framework Induced Synthesis of Single-Atom Dispersed Fe-N-C Acidic ORR Catalyst and Its in Situ Reduced Fe-N4 Active Site Identification Revealed by X-ray Absorption Spectroscopy. *ACS Catalysis* **2018,** *8* (4), 2824-2832.

47. Zhang, L.; Wang, A.; Wang, W.; Huang, Y.; Liu, X.; Miao, S.; Liu, J.; Zhang, T., Co–N–C Catalyst for C–C Coupling Reactions: On the Catalytic Performance and Active Sites. *ACS Catalysis* **2015,** *5* (11), 6563-6572.

48. Niu, W.; Yang, Y., Amorphous MOF Introduced N-Doped Graphene: An Efficient and Versatile Electrocatalyst for

Zinc–Air Battery and Water Splitting. *ACS Applied Energy Materials* **2018,** *1* (6), 2440-2445.

49. Wang, Z.; Jin, H.; Meng, T.; Liao, K.; Meng, W.; Yang, J.; He, D.; Xiong, Y.; Mu, S., Fe, Cu-Coordinated ZIF-Derived Carbon Framework for Efficient Oxygen Reduction Reaction and Zinc–Air Batteries. **2018,** *28* (39), 1802596.

50. Zhao, Y.; Lai, Q.; Zhu, J.; Zhong, J.; Tang, Z.; Luo, Y.; Liang, Y., Controllable Construction of Core–Shell Polymer@Zeolitic Imidazolate Frameworks Fiber Derived Heteroatom-Doped Carbon Nanofiber Network for Efficient Oxygen Electrocatalysis. **2018,** *14* (19), 1704207.

51. Khalid, M.; Honorato, A. M. B.; Ticianelli, E. A.; Varela, H., Uniformly self-decorated Co3O4 nanoparticles on N, S co-doped carbon layers derived from a camphor sulfonic acid and metal–organic framework hybrid as an oxygen evolution electrocatalyst. *Journal of Materials Chemistry A* **2018,** *6* (25), 12106-12114.

52. Zhao, Y.; Nakamura, R.; Kamiya, K.; Nakanishi, S.; Hashimoto, K., Nitrogen-doped carbon nanomaterials as non-metal electrocatalysts for water oxidation. *Nature Communications* **2013,** *4*, 2390.

53. Meng, T.; Qin, J.; Wang, S.; Zhao, D.; Mao, B.; Cao, M., In situ coupling of Co0.85Se and N-doped carbon via one-step selenization of metal–organic frameworks as a trifunctional catalyst for overall water splitting and Zn–air batteries. *Journal of Materials Chemistry A* **2017,** *5* (15), 7001-7014.

54. Ma, T. Y.; Cao, J. L.; Jaroniec, M.; Qiao, S. Z., Interacting Carbon Nitride and Titanium Carbide Nanosheets for High-Performance Oxygen Evolution. **2016,** *55* (3), 1138-1142.

55. Zhao, Y.; Watanabe, K.; Hashimoto, K., Self-Supporting Oxygen Reduction Electrocatalysts Made from a Nitrogen-Rich Network Polymer. *Journal of the American Chemical Society* **2012,** *134* (48), 19528-19531.

56. Wang, F.; Hu, L.; Liu, R.; Yang, H.; Xiong, T.; Mao, Y.; Balogun, M. S.; Ouyang, G.; Tong, Y., Hybrid implanted hybrid hollow nanocube electrocatalyst facilitates efficient hydrogen evolution activity. *Journal of Materials Chemistry A* **2019,** *7* (18), 11150-11159.

57. Luo, Y.; Zhang, J.; Kiani, M.; Chen, Y.; Chen, J.; Wang, G.; Chan, S. H.; Wang, R., Synthesis of MOF-Derived Nonprecious Catalyst with High Electrocatalytic Activity for Oxygen Reduction Reaction. *Industrial & Engineering Chemistry Research* **2018,** *57* (36), 12087-12095.

58. Xuan, C.; Hou, B.; Xia, W.; Peng, Z.; Shen, T.; Xin, H. L.; Zhang, G.; Wang, D., From a ZIF-8 polyhedron to three-dimensional nitrogen doped hierarchical porous carbon: an efficient electrocatalyst for the oxygen reduction reaction. *Journal of Materials Chemistry A* **2018,** *6* (23), 10731-10739.

59. Yang, L.; Jiang, S.; Zhao, Y.; Zhu, L.; Chen, S.; Wang, X.; Wu, Q.; Ma, J.; Ma, Y.; Hu, Z., Boron-Doped Carbon Nanotubes as Metal-Free Electrocatalysts for the Oxygen Reduction Reaction. **2011,** *50* (31), 7132-7135.

60. Yang, D.-S.; Bhattacharjya, D.; Inamdar, S.; Park, J.; Yu, J.-S., Phosphorus-Doped Ordered Mesoporous Carbons with Different Lengths as Efficient Metal-Free Electrocatalysts for Oxygen Reduction Reaction in Alkaline Media. *Journal of the American Chemical Society* **2012,** *134* (39), 16127-16130.

61. Liu, Y.-R.; Hu, W.-H.; Han, G.-Q.; Dong, B.; Li, X.; Shang, X.; Chai, Y.-M.; Liu, Y.-Q.; Liu, C.-G., Novel CoP Hollow Prisms as Bifunctional Electrocatalysts for Hydrogen Evolution Reaction in Acid media and Overall Water-splitting in Basic media. *Electrochimica Acta* **2016,** *220*, 98-106.

62. Li, W.; Zhang, S.; Fan, Q.; Zhang, F.; Xu, S., Hierarchically scaffolded CoP/CoP2 nanoparticles: controllable synthesis and their application as a well-matched bifunctional electrocatalyst for overall water splitting. *Nanoscale* **2017,** *9* (17), 5677-5685.

63. Li, H.; Li, Q.; Wen, P.; Williams, T. B.; Adhikari, S.; Dun, C.; Lu, C.; Itanze, D.; Jiang, L.; Carroll, D.

L.; Donati, G. L.; Lundin, P. M.; Qiu, Y.; Geyer, S. M., Colloidal Cobalt Phosphide Nanocrystals as Trifunctional Electrocatalysts for Overall Water Splitting Powered by a Zinc–Air Battery. **2018,** *30* (9), 1705796.

64. Liang, Y.; Li, Y.; Wang, H.; Zhou, J.; Wang, J.; Regier, T.; Dai, H., Co3O4 nanocrystals on graphene as a synergistic catalyst for oxygen reduction reaction. *Nature Materials* **2011,** *10*, 780.

65. Li, Y.-J.; Cui, L.; Da, P.-F.; Qiu, K.-W.; Qin, W.-J.; Hu, W.-B.; Du, X.-W.; Davey, K.; Ling, T.; Qiao, S.-Z., Multiscale Structural Engineering of Ni-Doped CoO Nanosheets for Zinc–Air Batteries with High Power Density. **2018,** *30* (46), 1804653.

66. Chen, S.; Chen, S.; Zhang, B.; Zhang, J., Bifunctional Oxygen Electrocatalysis of N, S-Codoped Porous Carbon with Interspersed Hollow CoO Nanoparticles for Rechargeable Zn–Air Batteries. *ACS Applied Materials & Interfaces* **2019,** *11* (18), 16720-16728.

67. Liu, G.; Li, J.; Fu, J.; Jiang, G.; Lui, G.; Luo, D.; Deng, Y.-P.; Zhang, J.; Cano, Z. P.; Yu, A.; Su, D.; Bai, Z.; Yang, L.; Chen, Z., An Oxygen-Vacancy-Rich Semiconductor-Supported Bifunctional Catalyst for Efficient and Stable Zinc–Air Batteries. *Advanced Materials 0* (0), 1806761.

68. Liu, S.; Zhou, J.; Song, H., Thermal-exfoliated synthesis of N-rich carbon-based nanosheets from layered bulk crystals of a metal–hexamine framework. *Chemical Communications* **2018,** *54* (70), 9825-9828.

69. Ndifon, P.; O. Agwara, M.; G. Paboudam, A.; Yufanyi, D.; Ngoune, J.; Galindo, A.; Alvarez, E.; Mohamadou, A., *Synthesis, characterisation and crystal structure of a cobalt(II)-hexamethylenetetramine coordination polymer*. 2009; Vol. 34, p 745-750.

70. Liu, S.; Zhou, J.; Song, H., 2D Zn-Hexamine Coordination Frameworks and Their Derived N-Rich Porous Carbon Nanosheets for Ultrafast Sodium Storage. **2018,** *8* (22), 1800569.

71. Sumboja, A.; An, T.; Goh, H. Y.; Lübke, M.; Howard, D. P.; Xu, Y.; Handoko, A. D.; Zong, Y.; Liu, Z., One-Step Facile Synthesis of Cobalt Phosphides for Hydrogen Evolution Reaction Catalysts in Acidic and Alkaline Medium. *ACS Applied Materials & Interfaces* **2018,** *10* (18), 15673-15680.

72. Hájek, J.; Mäki-Arvela, P.; Toukoniitty, E.; Kumar, N.; Salmi, T.; Murzin, D. Y.; Červený, L.; Paseka, I.; Laine, E., The Effect of Chemical Reducing Agents in the Synthesis of Sol-Gel Ru-Sn Catalysts: Selective Hydrogenation of Cinnamaldehyde. *Journal of Sol-Gel Science and Technology* **2004,** *30* (3), 187-195.

73. Shamir, D.; Meyerstein, D.; Zilbermann, I.; Burg, A.; Albo, Y.; Shames, A. I.; Vainer, R.; Borojovich, E. J. C.; Yardeni, G.; Kornweitz, H.; Maimon, E., Copper(II) catalyses the reduction of perchlorate by both formaldehyde and by dihydrogen in aqueous solutions. *Journal of Coordination Chemistry* **2018,** *71* (16-18), 2905-2912.

74. Zhao, Y.; Shi, R.; Bian, X.; Zhou, C.; Zhao, Y.; Zhang, S.; Wu, F.; Waterhouse, G. I. N.; Wu, L.-Z.; Tung, C.-H.; Zhang, T., Ammonia Detection Methods in Photocatalytic and Electrocatalytic Experiments: How to Improve the Reliability of NH3 Production Rates? **2019,** *6* (8), 1802109.

75. Feng, Y.; Yu, X.-Y.; Paik, U., Nickel cobalt phosphides quasi-hollow nanocubes as an efficient electrocatalyst for hydrogen evolution in alkaline solution. *Chemical Communications* **2016,** *52* (8), 1633-1636.

76. Du, C.; Yang, L.; Yang, F.; Cheng, G.; Luo, W., Nest-like NiCoP for Highly Efficient Overall Water Splitting. *ACS Catalysis* **2017,** *7* (6), 4131-4137.

77. Ray, C.; Lee, S. C.; Jin, B.; Kundu, A.; Park, J. H.; Jun, S. C., Stacked Porous Iron-Doped Nickel Cobalt Phosphide Nanoparticle: An Efficient and Stable Water Splitting Electrocatalyst. *ACS Sustainable Chemistry & Engineering* **2018,** *6* (5), 6146-6156.

78. Mishra, I. K.; Zhou, H.; Sun, J.; Qin, F.; Dahal, K.; Bao, J.; Chen, S.; Ren, Z., Hierarchical CoP/Ni5P4/CoP

microsheet arrays as a robust pH-universal electrocatalyst for efficient hydrogen generation. *Energy & Environmental Science* **2018,** *11* (8), 2246-2252.

79. Zhou, L.; Shao, M.; Li, J.; Jiang, S.; Wei, M.; Duan, X., Two-dimensional ultrathin arrays of CoP: Electronic modulation toward high performance overall water splitting. *Nano Energy* **2017,** *41*, 583-590.

80. Mao, S.; Wen, Z.; Huang, T.; Hou, Y.; Chen, J., High-performance bi-functional electrocatalysts of 3D crumpled graphene–cobalt oxide nanohybrids for oxygen reduction and evolution reactions. *Energy & Environmental Science* **2014,** *7* (2), 609-616.

81. Li, G.; Wang, X.; Fu, J.; Li, J.; Park, M. G.; Zhang, Y.; Lui, G.; Chen, Z., Pomegranate-Inspired Design of Highly Active and Durable Bifunctional Electrocatalysts for Rechargeable Metal–Air Batteries. **2016,** *55* (16), 4977-4982.

82. Fu, J.; Hassan, F. M.; Zhong, C.; Lu, J.; Liu, H.; Yu, A.; Chen, Z., Defect Engineering of Chalcogen-Tailored Oxygen Electrocatalysts for Rechargeable Quasi-Solid-State Zinc–Air Batteries. **2017,** *29* (35), 1702526.